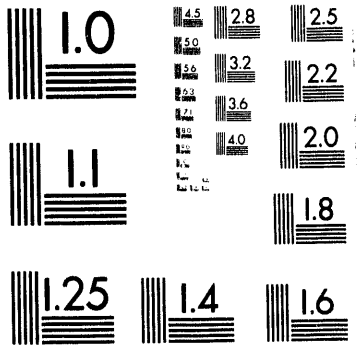
1.0
1.1
1.25
1.4
1.6
1.8
2.0
2.2
2.5
2.8
3.2
3.6
4.0
4.5
5.0
5.6

1 of 1

IS-T 1688

Terfenol: A Study of the Phase Equilibrium Diagram and the Solidification Process

by

Anderson, Mary

MS Thesis submitted to Iowa State University

Ames Laboratory, U.S. DOE

Iowa State University

Ames, Iowa 50011

Date Transmitted: December 7, 1993

PREPARED FOR THE U.S. DEPARTMENT OF ENERGY

UNDER CONTRACT NO. W-7405-Eng-82.

DISCLAIMER

TABLE OF CONTENTS

INTRODUCTION

A magnetic material in an alternating field will experience a mechanical vibration due to the magnetostriction, such as the humming (vibration) of a transformer. Most magnetostrictive materials exhibit a strain ($\Delta l/l$ or λ) on the order of 10^{-5}, but Terfenol has outstanding magnetostrictive properties at room temperature (Table 1). Some of the advantages of Terfenol for applications include: the largest room-temperature strain of any commercially produced magnetostrictive material, a response time in milliseconds, and a capability of hundreds of newtons of force (1). Further study of this alloy could improve the magnetostrictive response of this material.

Table 1 Magnetostriction coefficients of some cubic materials (2)

Material	$\lambda_{<100>}$ (10^6)	$\lambda_{<111>}$ (10^6)
Iron	21	-21
Nickel	-46	-24
Terfenol	90	1600

Terfenol is a rare earth-iron alloy that was first developed at the Naval Ordinance Lab because of its rare magnetostrictive properties. In fact, the name "Terfenol" is derived from Ter (terbium) -Fe (iron) -NOL (Naval Ordinance Lab). Terfenol is an alloy composed of the rare earth elements terbium and dysprosium combined with iron in a composition $Tb_xDy_{1-x}Fe_2$, where $x \approx 0.3$.

Rare earth elements have large magnetostrictions at low temperatures, but at room temperatures they are above the Curie temperature. Thus, by alloying these rare earth elements with the magnetic transition metals Ni, Co, and Fe, the Curie temperatures of the rare earth alloys are above room temperature and the magnetostrictions are present at room temperature. By alloying Tb and Dy with Fe such that the compound $Tb_xDy_{1-x}Fe_2$ ($x \approx 0.3$) forms, high strains at a low field are possible from the low anisotropy energy, which maximizes domain wall mobility and easy domain rotation at low fields (3). Figure 1 shows the dependence of the λ_{111} magnetostriction on the Tb:Dy ratio; note that at $x \approx 0.75$, the magnetostriction changes axes to the <100> crystallographic direction for $DyFe_2$ alloys.

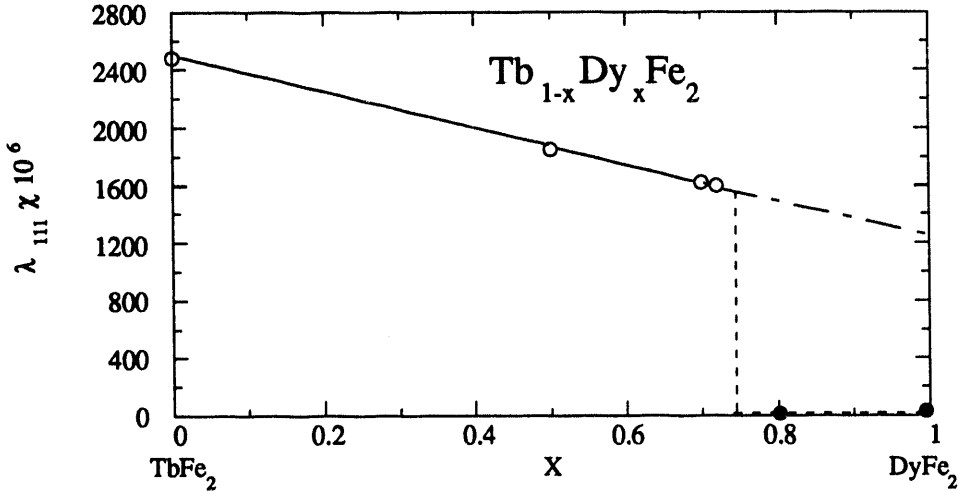

Figure 1 Plot of the magnetostriction $\lambda<111>$ of $Tb_{1-x}Dy_xFe_2$ at room temperature; open circles are $\lambda<111>$ and solid circles denote a region where no spontaneous $\lambda<111>$ exists (taken from Clark et al., 1976) (3)

Terfenol is generally considered to be the RFe_2 phase (where R = rare earth elements Tb or Dy); however, the overall composition of commercial Terfenol is usually $\approx RFe_{1.95}$. This is attributed to the fact that the RFe_2 phase is quite brittle, and small amounts of rare earth phase in the Terfenol matrix make the material more ductile without being too detrimental to the magnetostrictive properties. In this state, the material consists of two microconstituents: the RFe_2 compound and the rare earth rich microconstituent (4). Formation of the RFe_3 and other iron-rich phases are detrimental to the magnetostrictive properties of the alloy.

During the solidification of Terfenol alloys, the solid tends to grow with a dendritic growth front. The Terfenol dendrites grow with a sheet morphology having a <112> growth direction and a {111} plane aligned parallel with the sheet plane. The <112> dendrites characteristically have two or more parallel {111} twin planes along the center of the sheet plane, which are detrimental to the magnetostriction because they impede the domain wall motion during magnetization (4, 5). Since the largest magnetostriction of Terfenol occurs in the <111> direction, it would be desirable to have the crystal grow in the <111> direction, but the <112> dendrites form preferentially and large temperature gradients and slow solidification rates would be necessary to achieve a planar growth front during solidification.

A planar growth front could be achieved during solidification if the dendrites were suppressed. Dendrite growth requires constitutional supercooling; therefore, by creating a temperature gradient at the interface that is larger than the freezing temperature gradient due to the solute build-up at the interface, constitutional supercooling can be avoided and a planar growth front may be achieved (Figure 2). The solute build-up at the interface decreases the freezing temperature because of the inverse relationship between the freezing temperature (T_f) and the concentration (C) for systems where $x_S/x_l < 0$ (the composition of the solidus is smaller than the composition of the liquidus for a given temperature) (6).

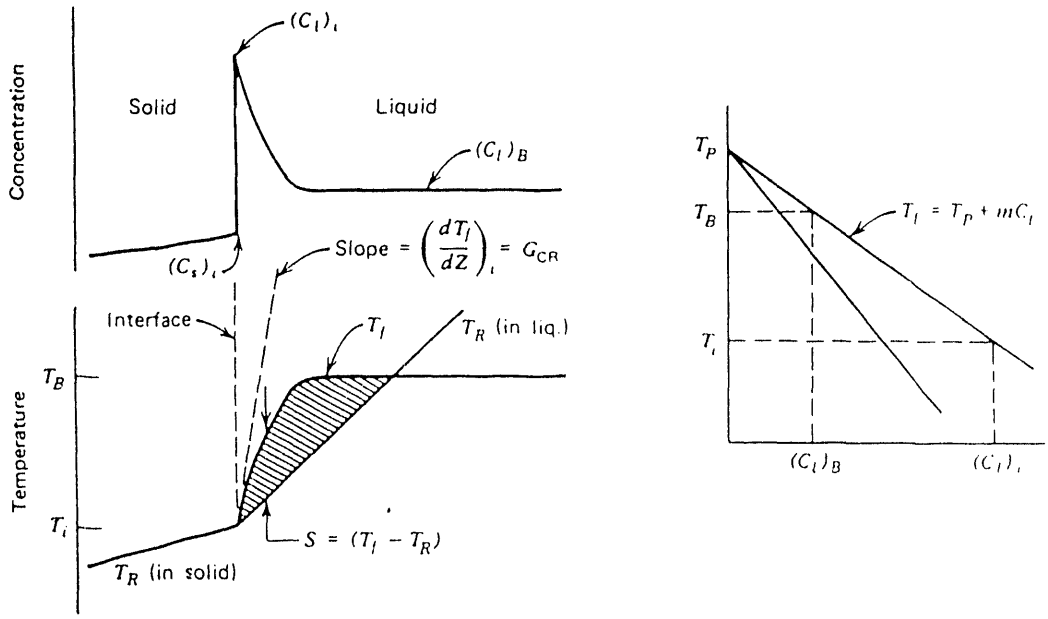

$(Cl)i$ = concentration of the liquid at the interface
$(C_S)i$ = concentration of the solid at the interface
$(Cl)B$ = concentration of the bulk liquid
G_{Cr} = critical temperature gradient
T_f = freezing temperature
T_R = real temperature
S = supercooling

Figure 2 The supercooled region (shaded area) produced by the solute build-up in alloy solidification in a positive temperature gradient provides a driving force for dendritic growth; a large temperature gradient is required in order to avoid supercooling to form a planar growth front (6)

From the equilibrium phase diagrams for Tb-Fe and Dy-Fe (Figures 4 and 5), the compositions of dendrites in equilibrium can be predicted, as shown for (a) Dy-Fe and (b) Tb-Fe in the Figure 3 below. The first model depicts the formation of a dendrite where the first phase forms from the liquid and subsequent phases form on the same dendrite. The second model shows different phases forming individual dendrites.

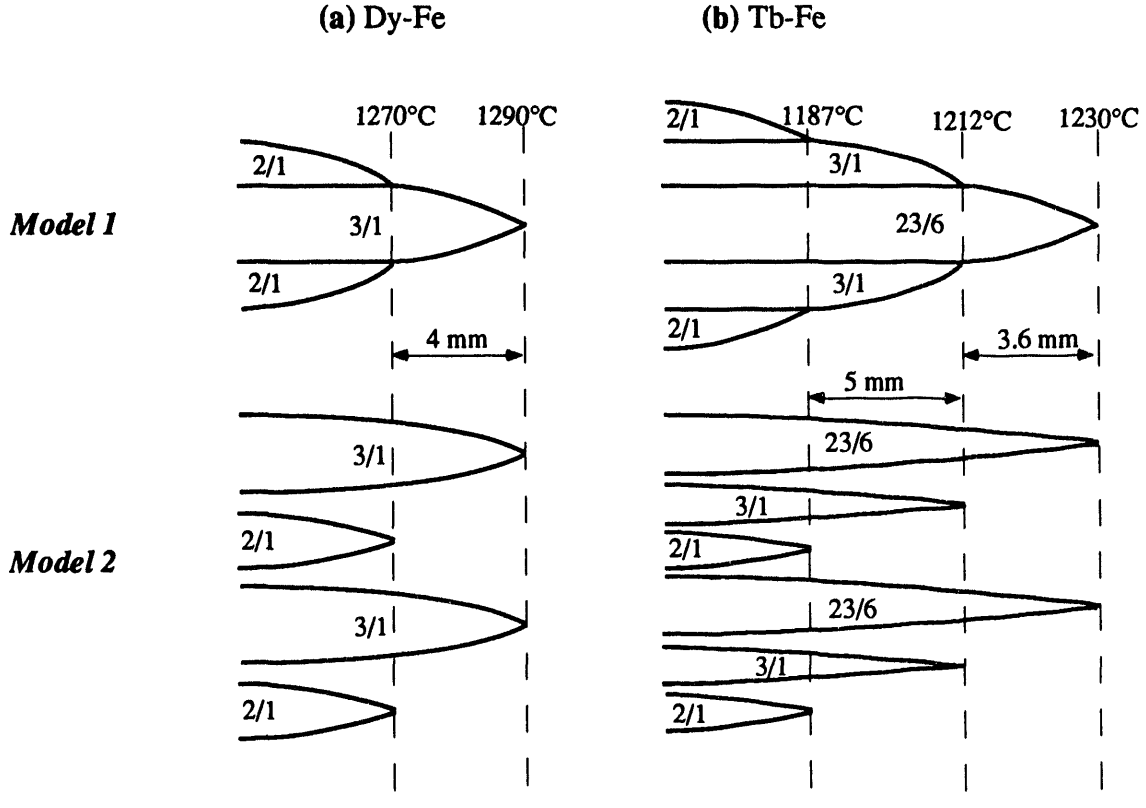

Figure 3 Composition of dendrites for Dy-Fe and Tb-Fe for same-phase dendrites and multi-phase dendrites

For a liquid of 2/1 (Fe/R) stoichiometry, the Tb-Fe equilibrium phase diagram (Figure 4) predicts that the R_6Fe_{23} phase will form first upon solidification, followed by the RFe_3 phase, and finally the RFe_2 phase will form. However, for the Dy-Fe system (Figure 5), a liquid composition of 2/1 (Fe/R) will yield the RFe_3 phase first and then the RFe_2 phase during solidification.

Although the equilibrium phase diagrams for Tb-Fe and Dy-Fe (Figures 4 and 5) predict that the RFe_2 phase would not form first for a liquid of 2/1 (Fe/R) composition, RFe_2 is the primary phase formed during solidification for $DyFe_2$ and $Tb_{.27}Dy_{.73}Fe_2$. Studies of RFe_2 samples have shown that float zone solidification at a growth rate of 140 μm/sec with both $DyFe_2$ and $Tb_{.27}Dy_{.73}Fe_2$ will form the RFe_2 phase with some eutectic, but $TbFe_2$ will form the RFe_3 phase surrounded by RFe_2. Additional work has indicated that growth rates exceeding 35 μm/sec in $Tb_{.27}Dy_{.73}Fe_2$ will form the RFe_2 compound directly from the liquid as a primary phase (7).

Faster solidification rates increase the undercooling of the liquid due to the latent heat of the alloy, and this undercooling may cause non-equilibrium precipitates to form. The solidification rate determines the amount of alloy that undergoes a phase change per unit time, and this phase change requires an amount of energy; this energy is achieved by undercooling the liquid to drive the reaction because thermodynamically the free energy (ΔG) is a function of the undercooling (ΔT).

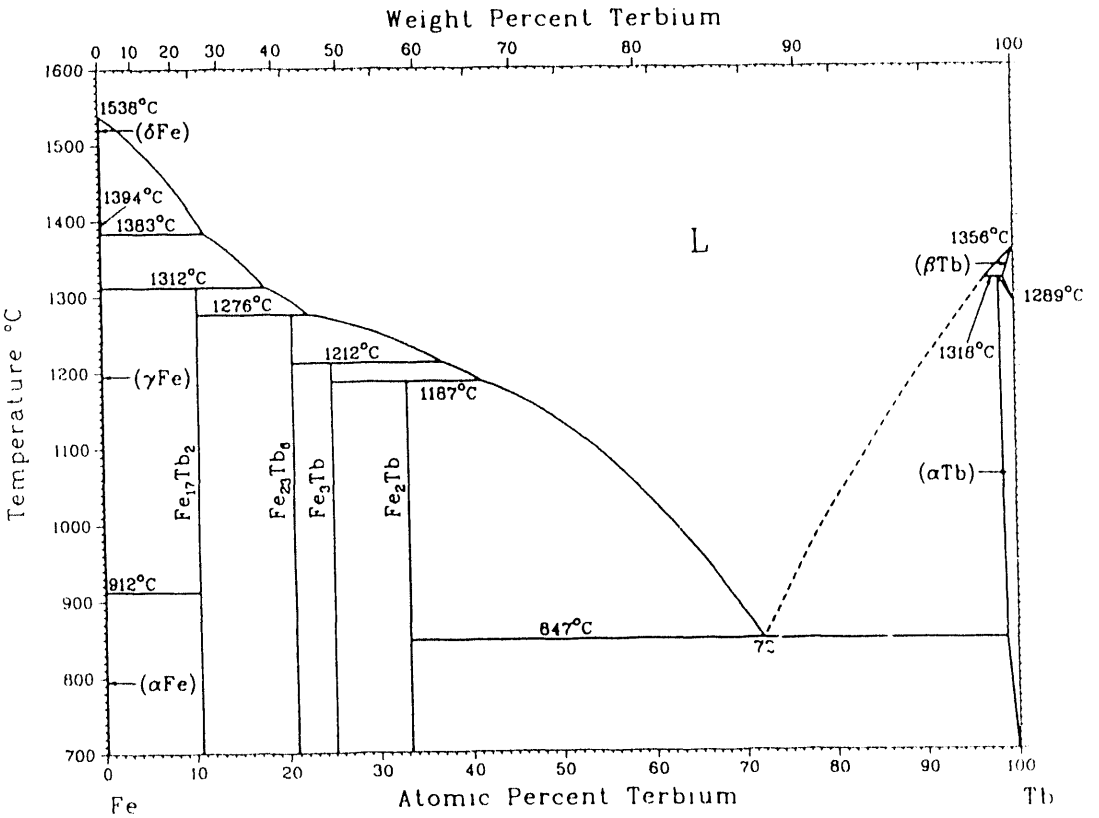

Figure 4 Terbium-iron equilibrium phase diagram (8)

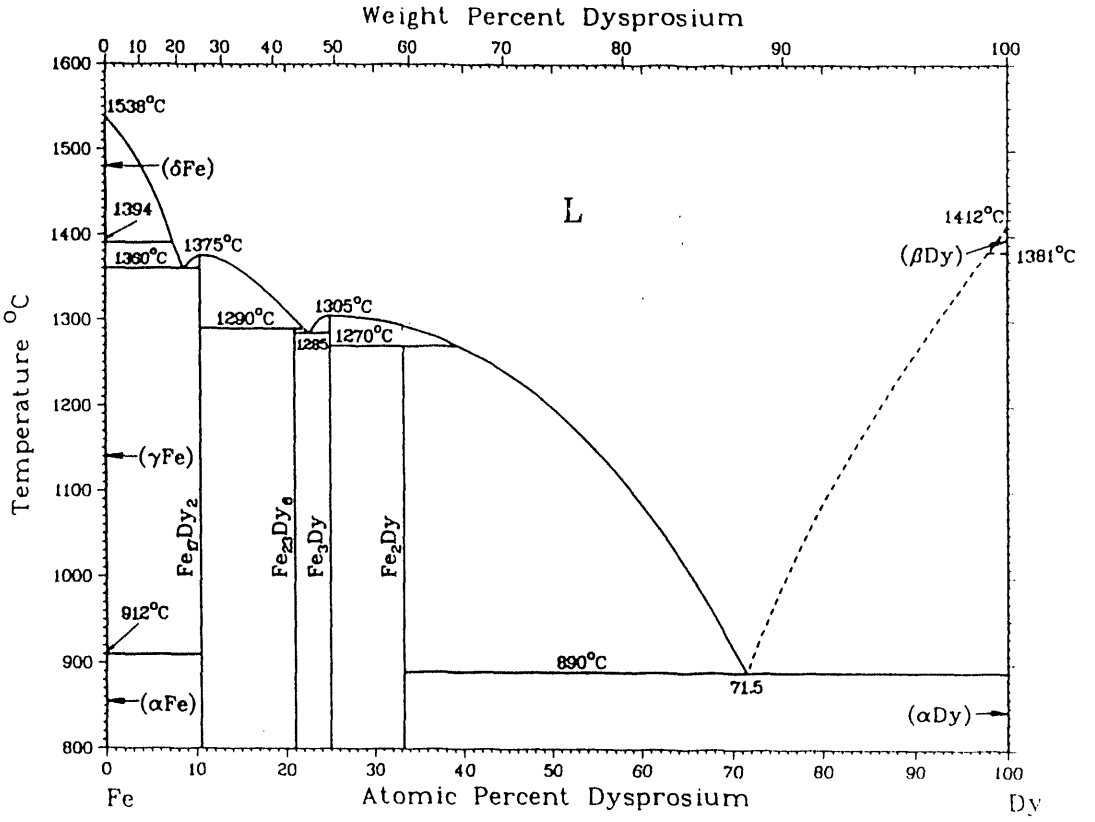

Figure 5 Dysprosium-iron equilibrium phase diagram (8)

Formation of the RFe_3 phase in Terfenol is detrimental to its magnetostrictive properties since the RFe_3 phase exhibits a smaller magnetostriction than the RFe_2 phase. In a sample of overall $RFe_{1.95}$ composition, microsegregation may occur in the dendrite, where the core of the dendrite is iron rich and the interdendritic area is rare earth rich; the iron rich region may lead to precipitation of the RFe_3 phase after solidification. However, an anneal at $\approx$ 950°C for 1 hour has proven effective for homogenization (elimination of the RFe_3 phase to produce an RFe_2 matrix with some undissolved rare earth metal). This heat treatment much improves the magnetostrictive response of the material because the RFe_2 phase exhibits superior magnetostrictive properties than the RFe_3 and other iron-rich phases(5).

With the given phase diagram for the dysprosium-iron system, free energy curves can be constructed to demonstrate that the RFe_2 phase will not precipitate out under equilibrium conditions, but may form under metastable conditions. Shown in Figure 6 are two free energy diagrams drawn at the temperature of the liquidus line at the 2/1 composition (T_2) and

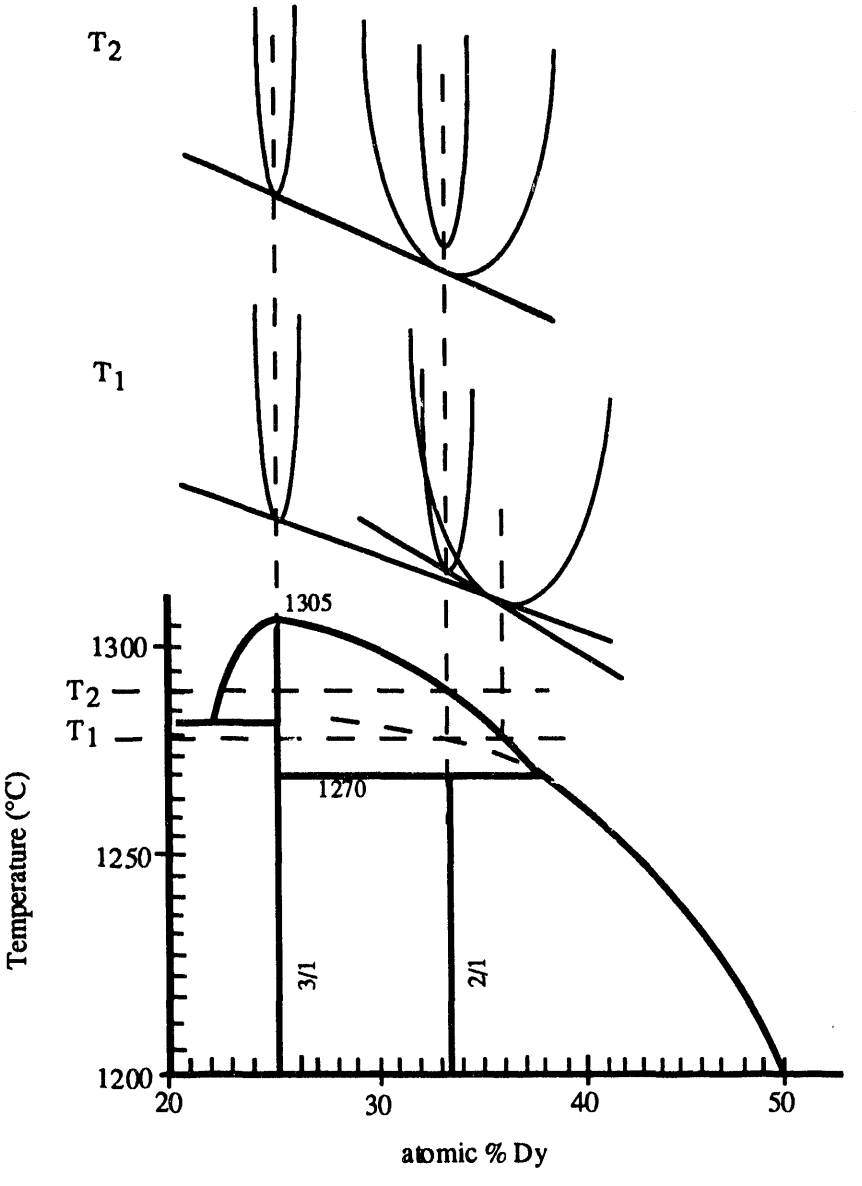

Figure 6 Possible free energy curves of the Dy-Fe phase diagram at T_1 and T_2

at a temperature just below that (T_1). The free energy diagram drawn at T_2 demonstrates that if the liquid of 2/1 composition began to solidify at the liquidus line (equilibrium conditions), the RFe_2 phase would not precipitate out because it has a higher free energy than the liquid; however, at T_1 it can be seen that the RFe_2 phase could form metastably, since the free energy change between the RFe_2 and RFe_3 phases is very small at the 2/1 composition. From these observations the conclusion can be reached that either the phase diagrams presented are not quite correct or that the solidification of the Terfenol dendrites is taking place under metastable conditions.

LITERATURE REVIEW

Several solidification techniques have been employed to grow Terfenol crystals; these include: Bridgman, Czochralski, and float zone solidification, to name a few of the most common ones. Terfenol produced for optimum magnetostriction would be high purity single crystals of RFe_2 oriented in the <111> crystallographic directions.

The Bridgman technique involves directional solidification of the Terfenol in an alumina or silica tube. Typically, the entire rod of Terfenol is melted (in a tube or container) and solidified directionally by lowering the Terfenol out of the furnace and through a cooling device. Since this technique requires that the molten Terfenol be in contact with alumina or silica at elevated temperatures for some time, especially if slow growth rates are used, contamination may occur in the Terfenol. Additionally, if large temperature gradients are achieved in order to try to get a planar growth front, further contamination is found because the molten Terfenol is in contact with the container at even higher temperatures.

The Czochralski solidification method involves using a seed of <111> oriented Terfenol in order to pull a <111> oriented single crystal of Terfenol from the melt. It has been attempted to grow <111> oriented Terfenol dendrites with <111> seeds, but this trial was unsuccessful because the <112> oriented grains formed near the seed interface and crowded out the <111> seeded grain (4).

Also, contamination of the Terfenol can occur in the crucible of molten Terfenol during solidification and macrosegregation may take place. Bi et. al. (9) have shown that contamination may be minimized by using an induction-heated cold crucible in Czochralski solidification. However, the Terfenol crystals grown in his system contained many Widmanstätten precipitates, which are detrimental to the magnetostrictive properties. In the same study, float zone solidification of the same composition of Terfenol yielded a sample with a higher density of defects, but with fewer interior oxide particles and twins.

Float zone solidification occurs when the Terfenol is melted at a small zone by coupling the Terfenol with a large RF field created by a coil surrounding the rod at the area to be melted. The molten zone created is quite small, and large temperature gradients can be achieved by controlling the distance between the zone and a cooling device. Numerous studies have been published which involve float zone solidification of Terfenol to try to grow single crystals .

Verhoeven et al. (4) did microstructural studies on Terfenol of composition $Tb_{0.3}Dy_{0.7}Fe_x$ (x = 1.80 to 1.99) solidified by Bridgman and float zone techniques. The

results indicated that the Terfenol solidified with a cellular to dendrite morphology in the <112> crystallographic direction along the rod axis. The dendrites formed as plates with their face parallel to the {111} plane; these planes contained two or more {111} twin boundaries along the center of the plate. Attempts to form <111> oriented rods from seeded float zone experiments failed. Rods of <112> orientation were formed as "single crystals" from seeded float zone experiments, but the crystals were not truly single due to the presence of parallel twin planes.

OBJECTIVE

Ultimately, our concern is to determine the growth characteristics of Terfenol and its dependence on solidification rate, temperature gradient, and stoichiometry. Several goals to further our knowledge were outlined at the beginning of this study:

(1) Verify the phase equilibria that is currently accepted for the systems $DyFe_2$ and $TbFe_2$, and establish the phase equilibria near the composition $Tb_{0.3}Dy_{0.7}Fe_2$.

(2) Establish that $Tb_{0.3}Dy_{0.7}Fe_2$ grows directly from the liquid, and that the reaction is occurring under metastable conditions.

(3) Evaluate whether or not we can grow $Tb_{0.3}Dy_{0.7}Fe_2$ under plane front conditions with a new RF (radio frequency) float zone apparatus.

(4) Determine whether or not we can grow <111> seeded crystals and produce <111> single crystals by elimination of dendrites employing growth methods capable of achieving high G/R (temperature gradient/solidification rate) ratios.

EXPERIMENTAL TECHNIQUES

Bridgman

Directional solidification (Bridgman technique) was conducted on cast iron, copper, and Terfenol. In the experiments, a Pt-Rh (type B) thermocouple was placed in the molten metal, just above the solid/liquid interface, and the temperature of the metal was recorded at 1 second intervals as the furnace and cold-finger of the directional solidification system were slowly moved up the axis of the molten metal, causing solidification of the metal around the thermocouple. The metal was contained in an alumina tube under an argon atmosphere. Solidification rates were controlled by a computer driven motor. Rates of 10, 25, and 50 μm/sec were used at furnace temperatures of 1300, 1350, 1400, 1450, and 1500 °C for four runs using a sample of Fe-4.3C-0.02S, and the same rates were used at furnace temperatures of 1250, 1300, 1350, and 1400 °C for one run using high purity copper. Terfenol samples of composition $Tb_{0.31}Dy_{0.69}Fe_{1.98}$ were also solidified ; the rates employed were 5, 10, 25, and 50 μm/sec at furnace temperatures of 1350 and 1400 °C. A diagram of this furnace is shown in Appendix A.

Float Zone Solidification

The float zone method is the solidification technique of interest due to its appealing characteristics for directional solidification: high temperature gradients , low impurity introduction, and minimal macrosegregation. In this system, the Terfenol is held in an argon atmosphere and is not in contact with anything, except at each end where the Terfenol rod is held. A coil around the Terfenol rod couples with a copper concentrator (water cooled) which creates its own field that couples with the Terfenol rod. The coil is held stationary as the Terfenol rod is moved up slowly by a computer driven motor, causing the zone to move down the rod axis. Also, the heating coil allows only a small band of metal to be melted at one time, causing a large temperature gradient and allowing little segregation. Thus, this set up may provide the proper conditions for plane front growth. A diagram of the float zone system is shown in Appendix A.

DTA Experimentation

Differential thermal analysis experiments were performed on Terfenol alloys of varying compositions in order to determine which phases are present at these compositions. An experiment done by McMasters involved the solidification of Dy_xFe_y samples where the dysprosium content was 22.5%, 26%, and 30% to determine which composition shows the 3/1 phase beginning to form. In a similar experiment, we solidified samples of R_xFe_y, where the rare earth content (R) of the alloy was 22.5, 26, and 30 atomic % (Table 2); the rare earth component had a Tb:Dy ratio of 3:7 in each alloy. The three Terfenol samples were arc melted into fingers and the microstructure of the samples was studied; the composition of each sample was verified using ICP (induction coupled plasma) analysis.

ICP Chemical Analysis

Three arc cast fingers, each with a different Terfenol composition, were sectioned and analyzed at each end and at the midsection (where the DTA samples were taken) in 1 to 2 gram samples using the ICP in order to determine the differences in composition from the target composition. The three Terfenol target compositions are listed in Table 2; the Dy:Tb ratio for each alloy was set to be 7:3 when the alloys were made.

The ICP test results have a ±3% error relative to the amount of each element present. Thus, included in the ICP results is the error associated with each alloy in each test specimen. The ICP results are given in Table 3. These results and their relative errors have been compared to the target compositions for each alloy (Table 2) to determine whether we can assume that the composition of the alloy is the target composition.

The difference between the target compositions and the ICP results can be compared to the error of the ICP analyses to determine how valid our target compositions are (Table 4); if the target composition are within the error of the analysis, then it is reasonable to assume

Table 2 Target compositions of the three arc cast Terfenol samples (RE stands for rare earth metals Tb and Dy)

Alloy	atom % Fe	atom % RE	atom % Dy	atom % Tb
Terf 22.5	77.5	22.5	15.75	6.75
Terf 26	74.0	26.0	18.20	7.80
Terf 30	70.0	30.0	21.00	9.00

that the target compositions are the compositions of the DTA samples. Note that the values for the target compositions at the midsection of each alloy in Table 4 are within error; since the DTA samples were extracted form the midsections of each casting, the DTA sample compositions for each alloy are assumed to be the target compositions.

Table 3 Results of the ICP chemical analysis from at each end and at the midsection of each of three arc cast Terfenol samples: Terf 22.5, Terf 26, and Terf 30

Alloy	area	atom % Fe	atom % Dy	atom % Tb
Terf 22.5	end #1	74.80±2.24	17.73±0.53	7.47±0.22
	end #2	79.53±2.39	14.38±0.43	6.09±0.18
	midsection	77.62±2.33	15.66±0.47	6.72±0.20
Terf 26	end #1	71.59±2.15	19.92±0.60	8.49±0.25
	end #2	79.06±2.37	14.67±0.44	6.27±0.19
	midsection	73.55±2.21	18.53±0.56	7.92±0.24
Terf 30	end #1	70.16±2.10	20.97±0.63	8.87±0.27
	end #2	71.30±2.14	20.22±0.61	8.48±0.25
	midsection	70.28±2.11	20.84±0.63	8.88±0.27

Table 4 The calculated difference between the target composition and the ICP composition compared with the error associated with the ICP test shows if we are within error; the values not within the ICP error are printed in bold

		± atom% Fe		± atom% Dy		± atom% Tb	
Alloy	area	diff.	± ICP	diff.	± ICP	diff.	± ICP
Terf 22.5	end #1	**-2.70**	±2.24	**1.98**	±0.53	**0.72**	±0.22
	end #2	2.03	±2.39	**-1.37**	±0.43	**-0.66**	±0.18
	midsection	0.12	±2.33	-0.09	±0.47	-0.03	±0.20
Terf 26	end #1	**-2.41**	±2.15	**1.72**	±0.60	**0.69**	±0.25
	end #2	**5.06**	±2.37	**-3.53**	±0.44	**-1.53**	±0.19
	midsection	-0.45	±2.21	0.33	±0.56	0.12	±0.24
Terf 30	end #1	0.16	±2.10	-0.03	±0.63	-0.13	±0.27
	end #2	1.30	±2.14	**-0.78**	±0.61	**-0.52**	±0.25
	midsection	0.28	±2.11	-0.16	±0.63	-0.12	±0.27

DTA Methods

Initially, differential thermal analysis (DTA) was performed using a Perkin Elmer DTA apparatus, which holds a small sample (≈ 100 mg) of crushed material in an alumina crucible in an argon atmosphere and measures the temperature difference between the sample of interest and a sample of alumina as the crucibles are heated at a standard rate of 0.167°C/sec. Thus, when the sample undergoes a thermal arrest during a phase transformation, the difference in temperature between the two samples becomes quite large. DTA was performed on high purity copper and iron, as well as some Terfenol samples with established compositions. This analysis was done for the comparison of the DTA results with the confirmed values to check the validity of the DTA system. The DTA results were reasonably congruent with expected results, indicating that the DTA method may be able to determine the phase diagram around the ternary Terfenol system. To better interpret the meaning of the DTA results, it was decided that metallographic analysis of solidified samples was required. Because the sample sizes of the Perkin-Elmer unit were too small, a DTA unit was constructed from the platinum furnace used with the directional solidification experiments. A diagram of our DTA unit is given in Appendix A.

In the construction of our own differential thermal analysis furnace, two type B thermocouples in alumina sheaths are used to determine the temperatures of a nickel standard and the Terfenol sample (≈2 grams) as the furnace temperature is incremented at a prescribed rate. The nickel and Terfenol samples are contained in alumina crucibles on pedestals that can be lowered out of the bottom of the furnace for quenching purposes. This setup is designed to be capable of quenching the sample in a liquid tin bath in order to observe the phases forming at critical temperatures. Also, the Terfenol samples are large enough that they may be mounted and polished for optical and SEM observation to determine the phase morphology and composition. The DTA experiments were performed with the Terf 22.5, Terf 26, and Terf 30 samples at cooling rates of 0.017 °C/sec, 0.083 °C/sec, furnace cooled (≈0.433 °C/sec), and helium quenched. Table 5 presents a summary of the experimental parameters used in the five sets of experiments carried out in the DTA apparatus.

The experiments using our DTA system consisted of heating the furnace under vacuum conditions to ≈800°C, then backfilling the furnace to 5 inches Hg (necessary because of the low vapor pressures of Tb and Dy) and heating the furnace to ≈1100°C. Next, the furnace was heated to 1250-1350°C at a prescribed rate while the temperature readings were taken, followed by cooling to ≈ 1150°C at a given rate with temperature readings, and then a reheat to 1250-1350°C (same as the first heat, except the first heats show the melting of

Table 5 DTA experimental parameters.

mount #	expt #'s	composition	Temp. range	heating rate	cooling rate	final cool rate
Set 1	1-79	Terf 22.5	1000-1320°C	0.083 °C/sec	0.083 °C/sec	furnace cool
	1-81	Terf 26	"	"	"	"
	1-83	Terf 30	"	"	"	"
Set 2	1-85	Terf 22.5	1000-1320°C	0.083 °C/sec	0.083 °C/sec	0.083 °C/sec
	1-87	Terf 26	"	"	"	"
	1-89	Terf 30	"	"	"	"
Set 3	1-91	Terf 22.5	1140-1340°C	0.083 °C/sec	0.083 °C/sec	0.083 °C/sec
	1-93	Terf 26	"	"	"	"
	1-95	Terf 30	"	"	"	"
Set 4	1-99	Terf 22.5	1100-1350°C	0.083 °C/sec	0.017 °C/sec	0.017 °C/sec
	1-101	Terf 26	"	"	"	"
	1-103	Terf 30	"	"	"	"
Set 5	1-107	Terf 26	1100-1350°C	0.083 °C/sec	0.083 °C/sec	0.083 °C/sec
	1-109	Terf 26	"	0.083 °C/sec	furnace cool	furnace cool
	1-111	Terf 26	"	0.083 °C/sec	0.017 °C/sec	0.017 °C/sec
	1-113	Terf 26	"	0.083 °C/sec	Quench	Quench

phases from the arc cast metal and the second heating should show the same phases that formed on cooling at the given rate). At the peak temperature, the thermocouple is removed from the molten metal, and the sample is cooled at the same rate as the first cool so that the microstructure of the DTA sample reflects the thermal events recorded.

Metallography

The DTA samples were mounted, polished, and etched for optical and SEM examination in order to determine the phases that formed and their morphology. The samples were generally polished using silicon carbide papers, then diamond polishing, and finally Linde A and B. Several etches were employed in order to be able to easily identify the phases optically: 2% nital, 5 % ferric chloride, Vilella's microetch, and boiling picric etch. The boiling picric etch gave the most outstanding differentiation between the phases. The samples were then observed microscopically and photomicrographs were taken to record the microstructure. Figure 8 describes the microstructure of a DTA sample.

Figure 8 Photomicrograph at 510X of a DTA sample from experiment 1-103 of Terf 30 (30 atomic % rare earth elements Tb and Dy) solidified at 0.017 °C/sec and etched with the boiling picric etch for 420 seconds showing RFe_3 dendrites and RFe_2 interdendritic (dark)

Scanning Electron Microscopy (SEM)

Scanning electron microscopy (SEM) was used with electron probe microanalysis (EPMA) for a quantitative analysis to determine the compositions of dendrites and other phases present in the Terfenol DTA samples. Iron, dysprosium, terbium, and Terfenol standards were used in the quantitative analysis. The atom% Fe found for each phase was compared to the atom% Fe that would be present in each of the four phases (see Table 6) in order to determine which phase was present.

Table 6 Compositions of four phases found in the Terfenol samples.

Phase	Abbr.	At % Fe	At % Dy	At % Tb	At % RE
RFe_2	2/1	66.67	23.34	9.99	33.33
RFe_3	3/1	75.00	17.50	7.50	25.00
R_6Fe_{23}	23/6	79.31	14.48	6.21	20.69
R_2Fe_{17}	17/2	89.47	7.37	3.16	10.53

RESULTS AND DISCUSSION

Bridgman

Directional solidification (Bridgman technique) of iron, copper, and Terfenol was performed in order to determine the temperature gradients achievable with the system and in order to observe the quench interface to see what the growth front looks like (planar or dendritic). Initial experiments were conducted on iron and copper, and eventually we progressed to Terfenol.

Figures 9 and 10 show example plots of the temperature gradients (temperature versus distance) in the liquid and solid during solidification for cast iron and copper, respectively. Figure 11 shows the temperature gradient versus the furnace temperature for each solidification rate for both liquid and solid metal; these plots show the following relationships:

a) Increased furnace temperatures cause increased temperature gradients for both solid and liquid metal, for both iron and copper.

b) In cast iron, the temperature gradients for the solid are larger than the liquid temperature gradients, while the reverse is true for copper. (For cast iron, this indicates that the liquid is more conductive than the solid, which is an unusual case resulting from the presence of graphite in the solid)

c) For cast iron, the solid temperature gradients increase with increasing velocity, while the liquid temperature gradients decrease with increasing velocity. The relation is unclear for copper.

From the solid and liquid temperature gradients determined for a particular furnace temperature and solidification rate, the thermal conductivities of the solid and liquid metal can be calculated from manipulation of the heat flow balance equation. This information is useful because the relationship between the temperature gradient and velocity is derived, which can be used to determine the solidification velocity corresponding to the critical temperature gradient at which a planar growth front is achieved. A derivation of the relation is given in Appendix B.

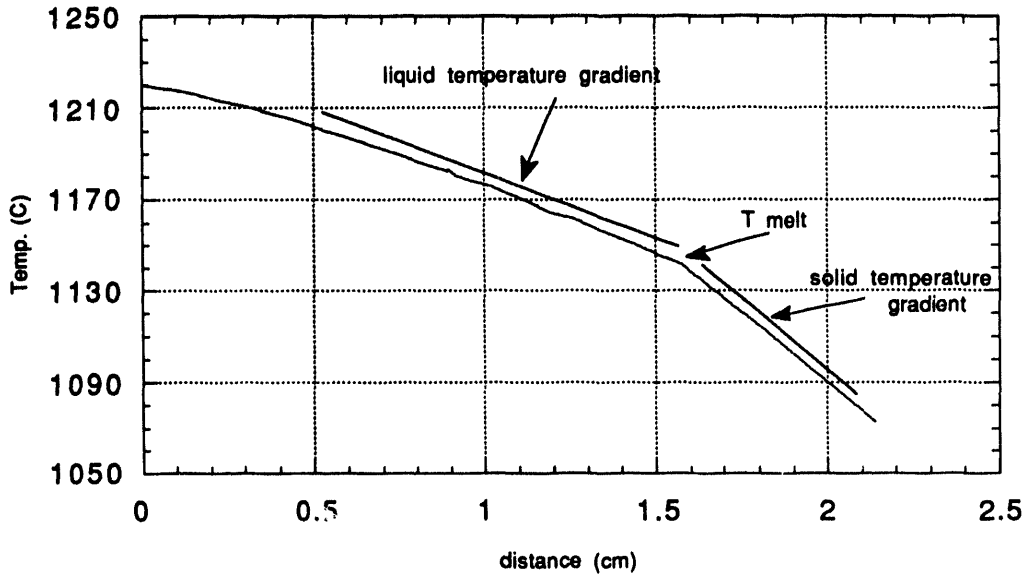

Figure 9 Example plot of temperature versus distance for cast iron at a furnace temperature of 1350°C and a solidification rate of 25μm/sec

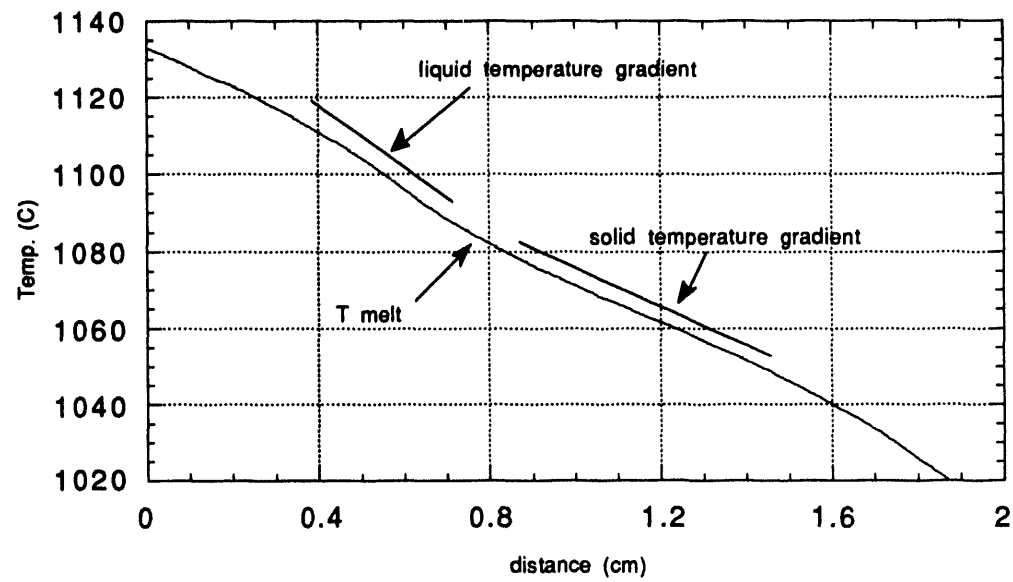

Figure 10 Example plot of temperature versus distance for high purity Cu at a furnace temperature of 1300°C and at a solidification rate of 25 μm/sec

(a)

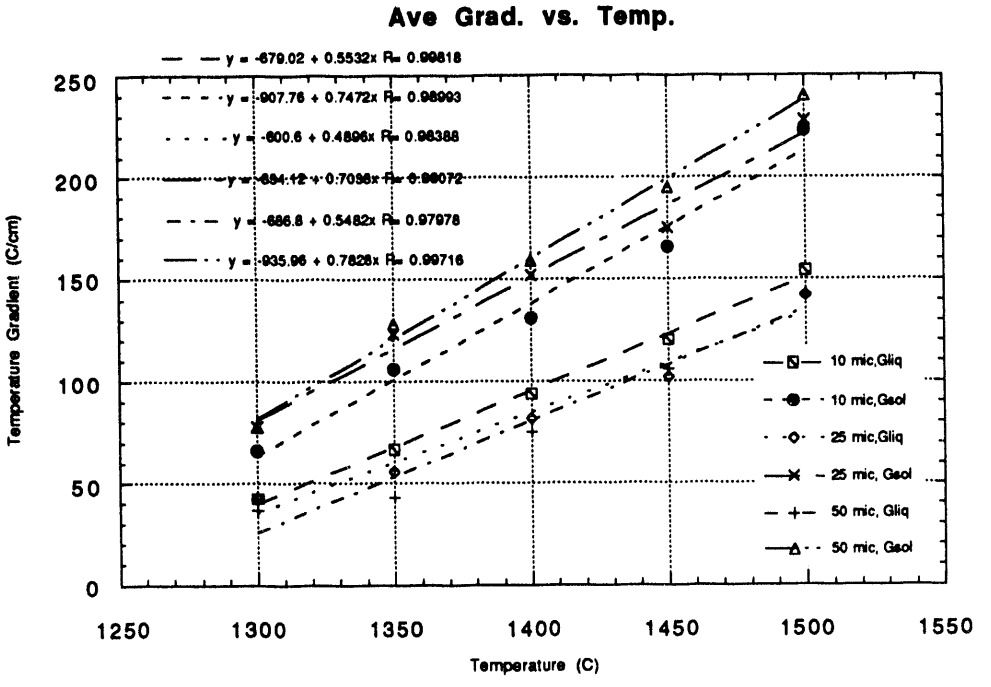

(b)

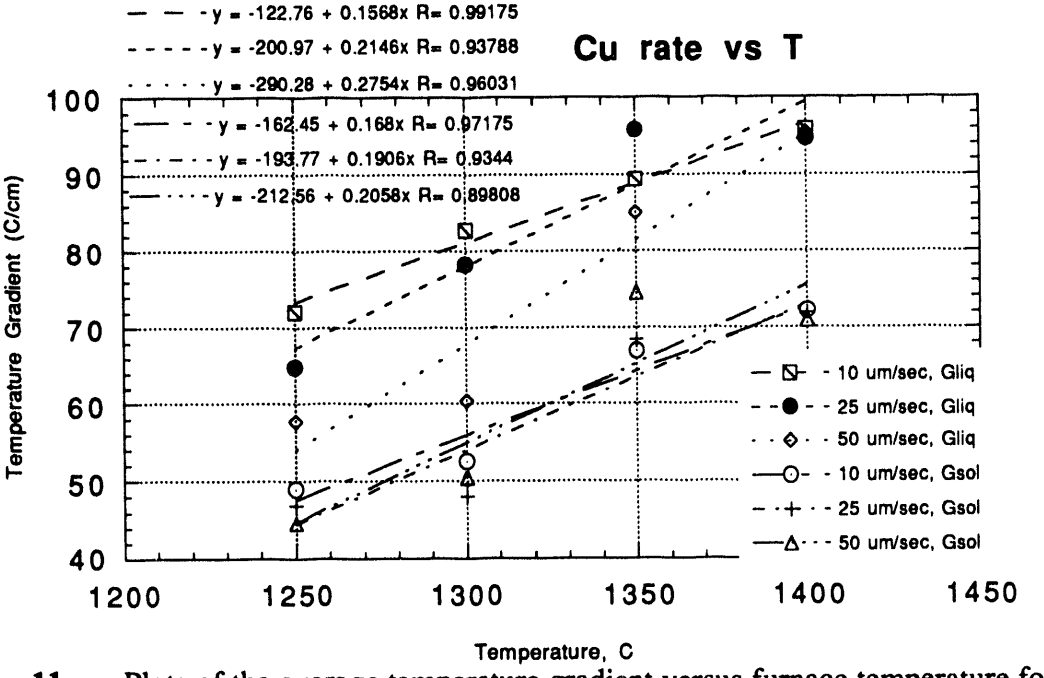

Figure 11 Plots of the average temperature gradient versus furnace temperature for solid and liquid (**a**) Fe-4.3C-0.02S and (**b**) high purity Cu .

Directional solidification using the Bridgman technique was attempted with a Terfenol sample of composition $Tb_{0.31}Dy_{0.69}Fe_{1.97}$. In order to achieve a planar growth front, large temperature gradients and slow solidification velocities are needed. However, Terfenol is easily oxidized, and since the Terfenol is contained in alumina (Al_2O_3), lower furnace temperatures and fast solidification rates are required in order to minimize the contamination of the Terfenol. Since the melting temperature of this alloy is ≈ 1240°C, furnace temperatures of 1350 and 1400°C with solidification rates of 5, 10, 25, and 50 μm/sec were employed and the temperature gradients were evaluated. Additionally, one run was conducted with a furnace temperature of 1350°C at a rate of 1 μm/sec and quenched in order to observe the interface. The dendrite formation was not suppressed even at this slow solidification rate, and evidence of oxidation was noted on the Terfenol samples. Also, the Terfenol samples were very difficult to remove from the alumina tubes without shattering due to their brittle nature. An example plot of temperature versus time is given in Figure 12; note the change in thermal conductivity at the melting temperature. More temperature gradient data on the Terfenol is given in Appendix B.

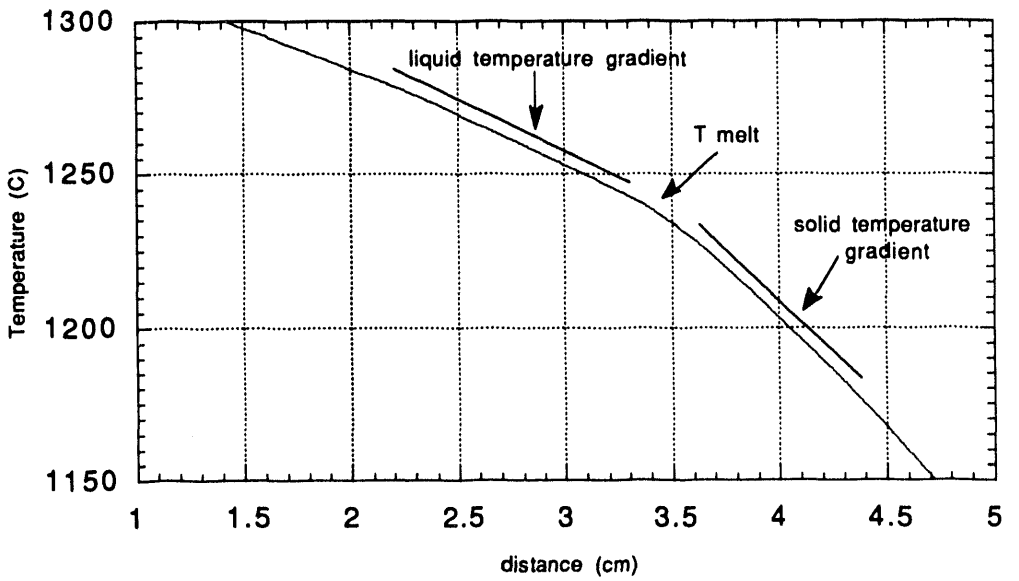

Figure 12 Plot of temperature versus time for a Terfenol sample of composition $Tb_{.31}Dy_{.69}Fe_{1.97}$ in experiment 1-51 with a furnace temperature of 1350°C and a solidification rate of 50 μm/sec

Float Zone Solidification

Development of the float zone apparatus was done by E. D. Gibson and is not the work of the author. The results of this work are presented here because of their close connection to the overall research program on Terfenol solidification. The float zone solidification experiments remain incomplete due to stability problems at the zone during experimentation. As the zone was melting and the rod was being moved at a constant rate of $\approx$ 10 μm/sec, the zone would begin to melt and the power would have to be turned down to prevent the rod from separating at the zone; the rod would then solidify and the power would have to be increased in order to have a molten zone. This process would continue because a stable zone could not be achieved. Part of the problem could be that the coupling between the field and the Terfenol changes as the Terfenol becomes molten and the rod diameter changes. Modifications to the setup, including changes in concentrator design, coil design, and power source, did not make the molten zone more stable. Solidification at faster rates may make the zone more stable, however the slow rates would be necessary to suppress dendrites (planar growth front).

Currently under construction is a new pancake coil that may concentrate the field more effectively. Also in design is a new type of concentrator modeled after the horizontal silver boat design.

Differential Thermal Analysis

The differential thermal analysis results indicate the temperatures at which thermal events (solidification or melting of phases) take place; from the size of the peak at the thermal event it is evident how much energy was absorbed or released during the phase transformation. Some of the DTA peaks overlap and it becomes difficult to differentiate between the thermal events. Some DTA plots for each composition at varying solidification rates are shown in Appendix C. The phase transformation is said to begin at the temperature of the steepest slope on the peak; this data has been arranged in Table 7 for each sample. The groupings of temperatures for the columns of Table 7 are thought to be the formation temperatures of the four phases; these temperatures were chosen because of the trend seen in the DTA results and for simplicity for correlation to the SEM phases found and phase solidification sequence from microstructure studies. The set 2 experiments were a repeat of set 1, with a final cool of 0.083 °C/sec instead of a furnace cool, and the DTA results were

quite similar. Sets 3 to 5 were heated to a higher furnace temperature than sets 1 and 2 to make sure that all of the R_2Fe_{17} phase was melted. Set 4 was solidified at a slower rate, 0.083 °C/sec. Set 5 consisted of all Terf 26 samples cooled at the various rates, because Terf 26 seemed to have the widest variation of microstructures depending on the solidification rate. The DTA plots are shown in Appendix C.

Table 7 Results of the DTA (Differential Thermal Analysis) experiments

Samples			DTA Thermal Events			
mount	samples	final cool rate (°C/min)	1220 to 1230 °C	1250 to 1260 °C	1275 to 1285 °C	1290 to 1300°C
Set 1	Terf 22.5	furnace cool		1255 °C	1280 °C	
	Terf 26	"	1220 °C	1250 °C	1280°C	
	Terf 30	"	1230 °C	1250 °C		
Set 2	Terf 22.5	0.083 °C/sec		1250 °C	1280 °C	
	Terf 26	"	1225 °C	1260 °C	1280 °C	
	Terf 30	"	1225 °C	1250 °C		
Set 3	Terf 22.5	0.083 °C/sec		1255 °C	1280 °C	1295 °C
	Terf 26	"	1230 °C	1255 °C	1275 °C	
	Terf 30	"	1230 °C	1250 °C		
Set 4	Terf 22.5	0.017 °C/sec		1254 °C	1282 °C	1300 °C
	Terf 26	"		1262 °C		
	Terf 30	"	1233 °C	1257 °C		
Set 5	Terf 26	0.017 °C/sec		1255 °C	1280 °C	
	Terf 26	0.083 °C/sec		1255 °C	1280 °C	
	Terf 26	furnace cool		1255 °C	1280 °C	

Metallography

From the etches of the various DTA samples, the morphology of the phases present becomes evident and the solidification sequence of the phases can be determined. The etchant that distinguished all four phases (RFe_2, RFe_3, R_6Fe_{23}, and R_2Fe_{17}) the best was

the boiling picric etch for ≈ 420 seconds. Table 8 shows the phases present for each sample. A series of photomicrographs for the DTA samples is shown in Appendix D.

From the photomicrographs, the solidification sequence of the phases is deduced from the phase morphology. For example, the photomicrograph in Appendix D of Terf 22.5 in experiment 1-83 (furnace cooled), shows that the matrix of the sample is RFe_3, the dendrites are R_2Fe_{17}, and the faceted phase is R_6Fe_{23}. The dendritic phase forms from supercooling

Table 8 Phases present by etching and their relative structures and approximate amount present; verification has been performed via EPMA on an SEM

		17/2	**23/6**	**3/1**	**2/1**
Set #1	Terf 22.5	≈30%, dendrite	≈30%, faceted	≈40%, matrix	---
(furnace	Terf 26	interdendritic	some facets	matrix	---
cool)	Terf 30	---	some facets	≈50%, dendrite	≈50%, dendrite
Set #2	Terf 22.5	≈30%, dendrite	≈30%, faceted	≈40%, matrix	---
(5 °C/min)	Terf 26	interdendritic	some facets	matrix	---
	Terf 30	---	some facets	≈50%, dendrite	≈50%, dendrite
Set #3	Terf 22.5	≈30%, dendrite	≈30%, faceted	≈40%, matrix	---
(5 °C/min)	Terf 26	interdendritic	some facets	matrix	---
	Terf 30	---	some facets	≈50%, dendrite	≈50%, dendrite
Set #4	Terf 22.5	≈40%, dendrite	≈40%, matrix	≈20%, ?	---
(1 °C/min)	Terf 26	interdendritic	≈20%, faceted	≈75%, matrix	---
	Terf 30	---	few facets	≈50%, dendrite	≈50%, dendrite
Set #5	Terf 26 (1 °C/min)	---	≈50%, faceted	≈5%, peritectic	≈45%, peritectic
	Terf 26 (5 °C/min)	---	≈30% , faceted	≈65%, dendrite	5%interdendritic
	Terf 26 (furnace cool)	---	≈20%, faceted	≈77%, dendrite	3%interdendritic
	Terf 26 (Quench)	---	---	≈99%, dendrite	---

at the solid/liquid interface (Figure 2). As the first phase forms (R_2Fe_{17} dendrites), the composition of the liquid changes along the liquidus line of the phase equilibrium diagram. Eventually, the composition of the liquid changes so that it is more favorable for another phase to form (R_6Fe_{23} faceted phase). This phase grows until again the liquid composition has changed such that a third phase (RFe_3) is formed, and the remaining liquid solidifies as the RFe_3 phase.

The faceted phase grows by motion of small ledges, where atoms attach themselves only at the ledges, as shown in Figure 13 (a). The faceting planes of the faceting interface occur on preferred crystallographic planes (6). For non-faceting solidification, atoms attach themselves all along the solid/liquid interface, as shown in Figure 13 (b).

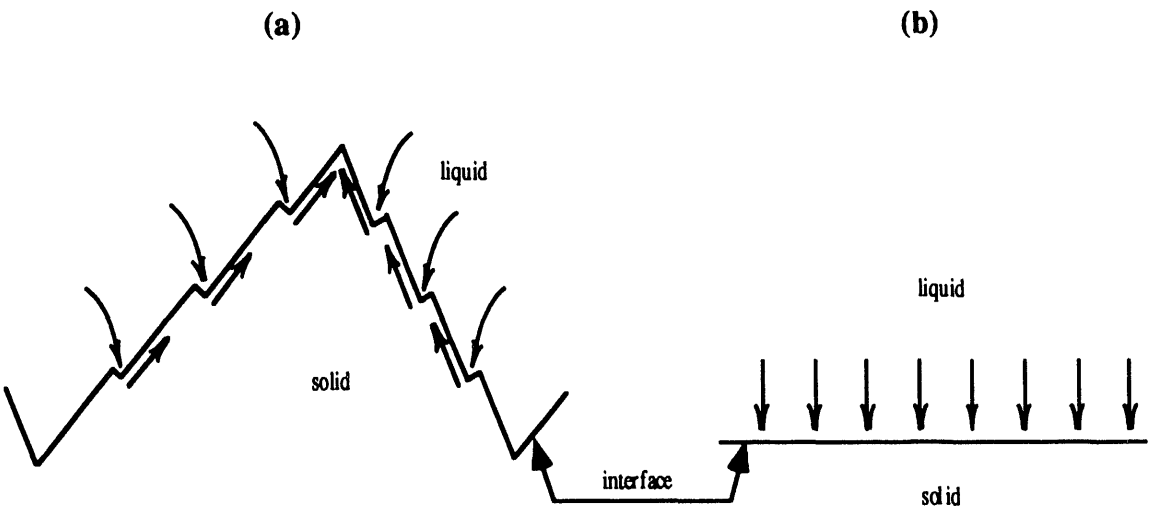

Figure 13 Atomic attachment at **(a)** the faceted interface and **(b)** the non-faceted interface (6)

Peritectic solidification occurred in the DTA samples of Terf 22.5 and Terf 26 that were solidified at a rate of 0.017 °C/sec (Figures 37 and 38 in Appendix D). Peritectic reactions involve the liquid reacting with one phase to form a second phase ($L + \alpha \rightarrow \beta$), as shown in Figure 14 (10).

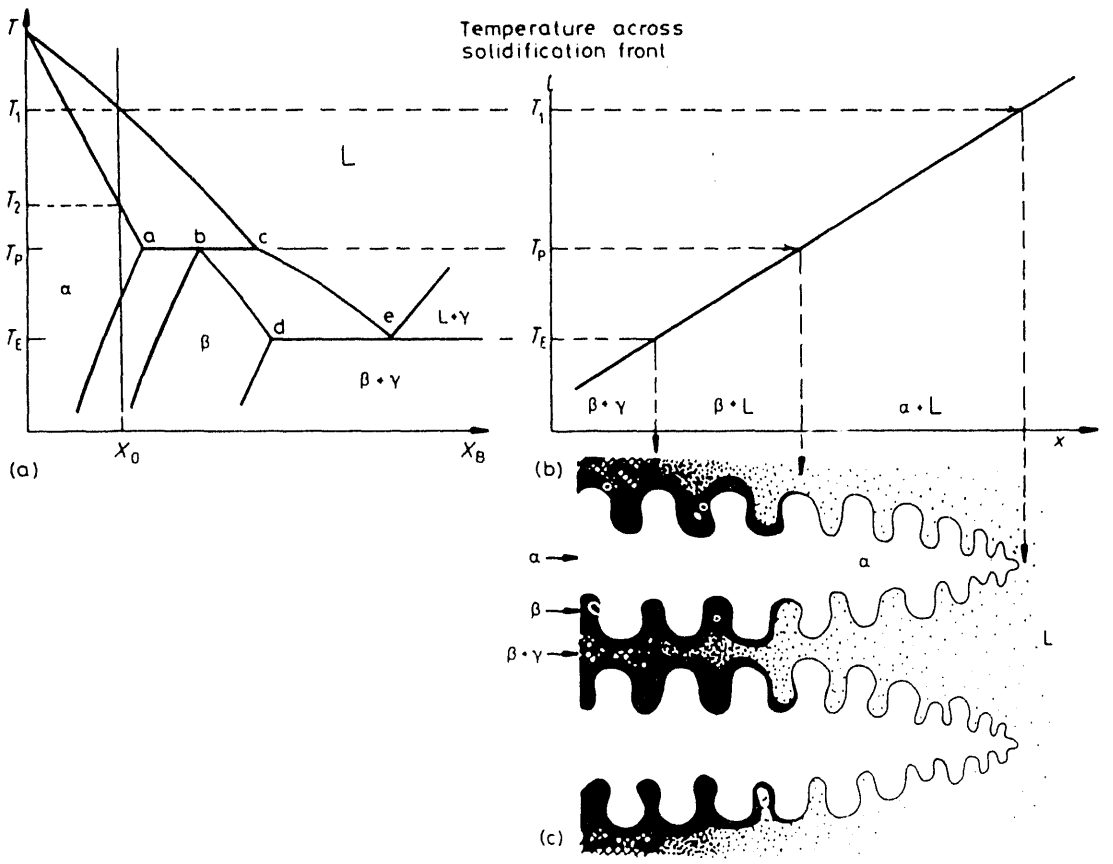

Figure 14 Peritectic solidification in a temperature gradient (10)

Scanning Electron Microscopy

The results of the SEM analysis show the phases present in each sample determined by electron probe microanalysis (EPMA). The compositions were determined for the phases in an area where the sample had been optically photomicrographed, so that the composition could be directly related to the phases observed. Table 9 presents a summary of the phases identified with EPMA in experiment sets 1, 2, 4, and 5. These results are the basis for the classification presented in Table 8.

Table 9 SEM results from EPMA performed on the DTA samples from experiment sets 1, 2, 4, and 5 (set 3 was not evaluated on the SEM)

			Phases			
set #	final cool rate	sample	RFe_2	RFe_3	R_6Fe_{23}	R_2Fe_{17}
Set 1	furnace cool	Terf 22.5		X	X	X
		Terf 26		X		X
		Terf 30	X	X		
Set 2	0.083 °C/sec	Terf 22.5		X	X	X
		Terf 26	X	X	X	
		Terf 30	X	X		
Set 4	0.017 °C/sec	Terf 22.5		X	X	X
		Terf 26		X	X	X
		Terf 30	X	X	X	
Set 5	0.017 °C/sec	Terf 26	X	X	X	
	0.083 °C/sec	Terf 26	X	X	X	
	furnace cool	Terf 26	X	X	X	
	Quench	Terf 26		X		

Correlation

The results of the thermal events detected by differential thermal analysis and the phases present determined by the study of photomicrographs and from the quantitative analysis on the SEM for the three Terfenol compositions can be correlated to understand the solidification process of Terfenol and its dependence on stoichiometry. By observation of the morphology of the phases present, the solidification sequence at each composition and solidification rate can be determined. From this information and the DTA results, a pseudobinary phase diagram could be constructed for Fe and R (Dy:Tb =3:7).

The thermal events from the DTA should correspond to the phases determined in the SEM. However, the first set of data had a furnace cool, which occurs much faster than the 0.083 °C/sec DTA analysis, thus forming non-equilibrium phases that did not appear in the DTA results. Additionally, the first and second sets of data were not heated to a temperature

high enough to melt one of the phases (R_2Fe_{17}) and thus the phase did not appear in the DTA results. The third and fourth sets of data were heated to a point where the fourth phase was detectable. The fourth set of data was cooled at 0.017 °C/sec to get sharper peaks so that smaller peaks would not be overlooked due to overlapping of a larger, broader peak.

The data in Tables 7 to 9 may be correlated to identify the melting temperatures found for the four phases forming in these alloys; these results are presented in Table 11. The melting temperature for the R_2Fe_{17} phase was not determined, because melting of the Terf 30 alloy melted the R_2Fe_{17} phase on the liquidus line of the phase diagram.

Table 11 Correlation of the phases found in the SEM to the thermal events of the DTA

Phase	T. melt
RFe_2	≈1225 °C
RFe_3	≈1255 °C
R_6Fe_{23}	≈1280 °C

Phase Diagram

From the experimental results a pseudobinary phase diagram can be derived. The temperatures at which each phase forms for the three Terfenol compositions has been determined with DTA experimentation. From the analysis of the morphology of the phases in the photomicrographs, the solidification sequence was determined. The results of EPMA on the SEM revealed the phases present. The evaluation of the results led to the phase diagram in Figure 15. This diagram agrees with the solidification structures that have been observed in the DTA samples. The microstructures approach equilibrium morphologies as they are cooled at slower rates. Thus, Terf 22.5 and Terf 26 displayed peritectic reactions at a 0.017 °C/sec cooling rate, and the phase diagram constructed predicts peritectics between the R_2Fe_{17} phase and the R_6Fe_{23} phase, as well as between the R_6Fe_{23} and RFe_3 phases.

It is of interest to note that the proposed phase diagram in Figure 15 (for R-Fe where R has a constant Dy:Tb ratio of 7:3)more closely resembles the construction of the Tb-Fe phase diagram (Figure 4) than the Dy-Fe phase diagram (Figure 5), even though there is considerably more Dy in the alloy than Tb.

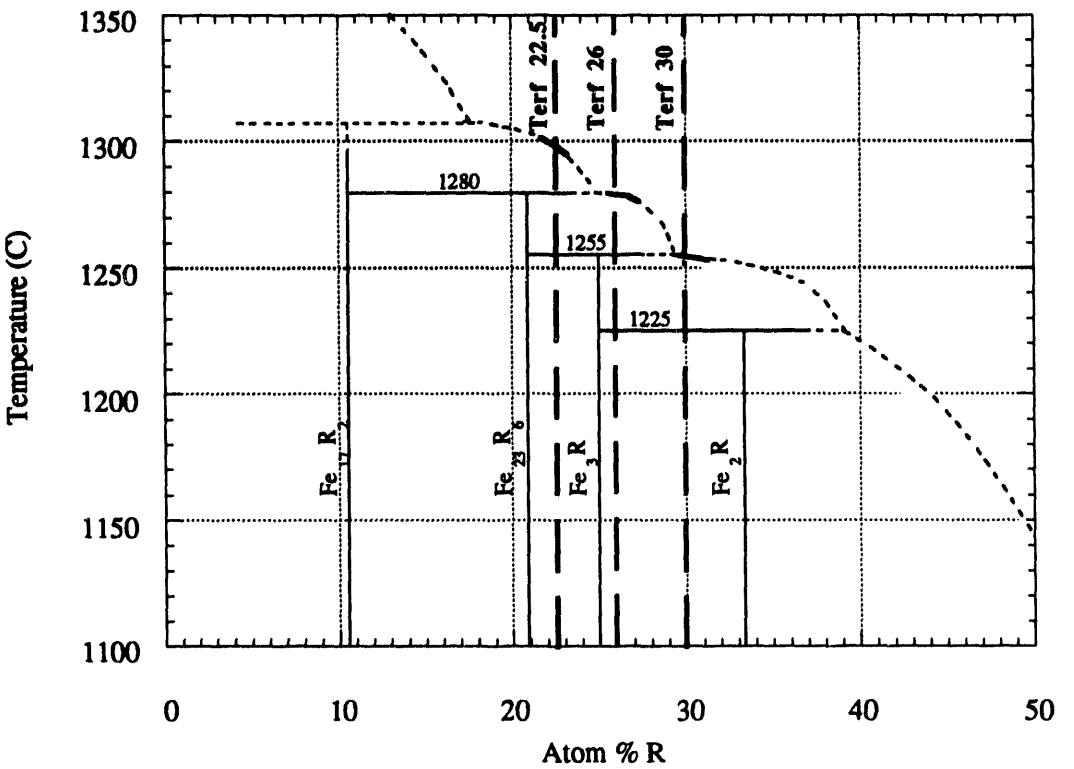

Figure 15 Diagram of a possible Fe-R (Dy:Tb = 7:3) phase diagram from experimental data

For comparison, an Fe-R (Dy:Tb = 7:3) phase diagram has been constructed from the Dy-Fe and Tb-Fe phase diagrams by calculations assuming a linear relationship between phases on the diagrams. This diagram is an isopleth of the Tb-Dy-Fe ternary phase diagram. The melting temperature for each phase was determined by weighing the respective melting temperatures according to the Dy:Tb ratio as follows:

$$T_{melt}\text{ (R-Fe phase)} = 0.7*T_{melt}\text{ (Dy-Fe phase)} + 0.3*T_{melt}\text{ (Tb-Fe phase)}$$

This technique assumes that there is a linear relation as the alloy composition changes. The calculated results for the melting temperatures of the R-Fe phases (where R = Dy:Tb = 7:3) are listed in Table 12.

The same method of calculation was used in determining the compositions at which two phases are in equilibrium with the liquid. The results of the composition calculations are given in Table 13. The calculation format is as follows:

$$\text{Comp}_{\text{R-Fe}}(\ell, \text{phase 1, phase 2}) = 0.7*\text{Comp}_{\text{Dy-Fe}}(\ell, \text{phase 1, phase 2}) + 0.3*\text{Comp}_{\text{Tb-Fe}}(\ell, \text{phase 1, phase 2})$$

An R-Fe (Dy:Tb = 7:3) phase diagram based on our assumptions of a linear relation between the Dy-Fe alloys and the Tb-Fe alloys was constructed using the data in Tables 12 and 13; this diagram is shown in Figure 16. A comparison of the phase diagram from experimental results (Figure 15) to Figure 16 reveals that the solidification temperatures for the phases vary, but both diagrams show peritecrtics between phases. Also, Figure 16 shows that the R_2Fe_{17} phase would not be present in Terf 22.5 under equilibrium conditions.

Table 12 Calculation of the melting temperatures for the R-Fe phases from the Dy-Fe and Tb-Fe phase diagrams

	Melting Temperature (°C)		
Phase	Dy-Fe	Tb-Fe	R-Fe (Dy:Tb = 7:3)
RFe_2	1270	1187	1245
RFe_3	1305	1212	1277
R_6Fe_{23}	1290	1276	1285
R_2Fe_{17}	1360	1312	1345

Table 13 Calculation for the R-Fe phase diagram of the composition at which the liquid is in equilibrium with two phases. Data from the Tb-Fe and Dy-Fe phase diagrams in Figures 4 and 5, respectively

	Composition, atom % rare earth metal		
Phase	Dy-Fe	Tb-Fe	R-Fe (Dy:Tb = 7:3)
RFe_2	39.0	41.2	39.7
RFe_3	22.5	37.0	26.9
R_6Fe_{23}	21.7	22.6	22.0
R_2Fe_{17}	8.8	17.8	11.5

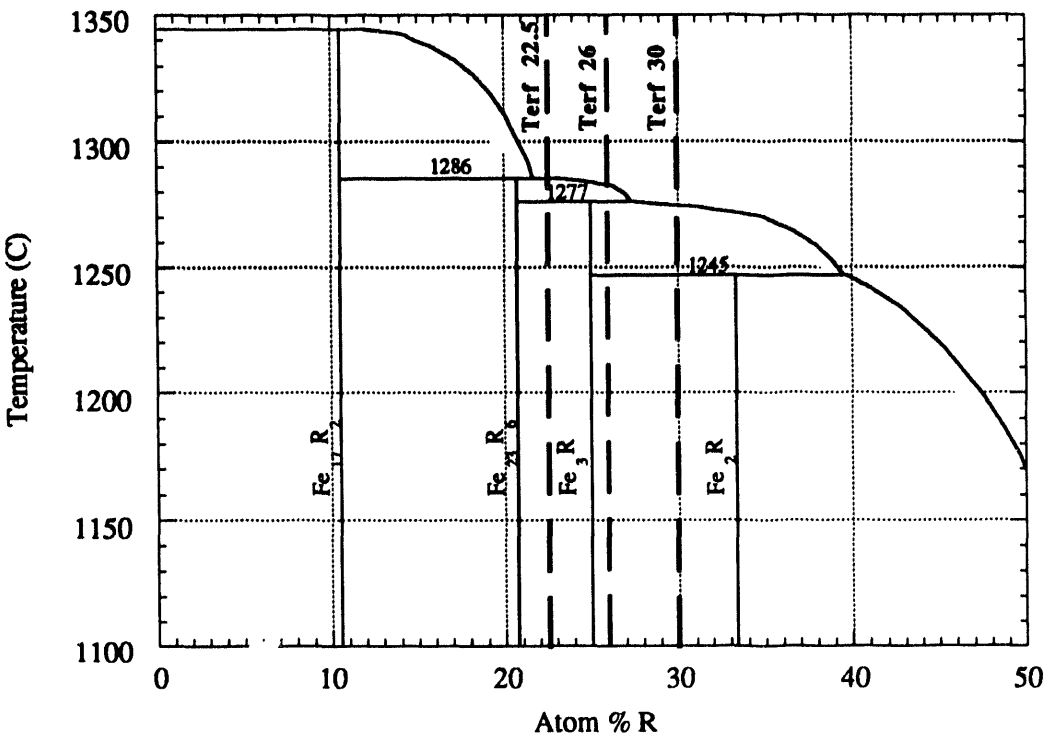

Figure 16 R-Fe phase diagram (where R has a constant Dy:Tb ratio of 7:3) constructed from calculations involving the Dy-Fe and Tb-Fe phase diagrams

A ternary diagram of Fe-Dy-Tb system looks like a triangle with one side being the Dy-Fe phase diagram, one side as the Tb-Fe phase diagram, and one as the Dy-Tb phase diagram; the volume of the ternary diagram consists of Tb-Dy-Fe phases. Since Tb and Dy are so similar, it is expected that there is a linear change from the phases of the Tb-Fe phase diagram to the phases of the Dy-Fe phase diagram. The ternary diagram from above (Figure 17) shows the assumed linear relationships and where they cross over from eutectic ($DyFe_3$ and Dy_6Fe_{23} eutectic and Dy_2Fe_{17} and Fe eutectic on the Dy-Fe phase diagram) to peritectic (on the Tb-Fe phase diagram).

For example, a line has been drawn from 63 at % on the Tb-Fe phase diagram to 77.5 at % Fe on the Dy-Fe phase diagram; this line symbolizes the liquid/RFe_3/R_6Fe_{23}

equilibrium points from Tb-Fe to Dy-Fe. Just to the right of the 0.7Dy/0.3Tb line, the RFe_3 and R_6Fe_{23} trough crosses the RFe_3 composition (75 at% Fe), which means that if the trough is between the RFe_3 and R_6Fe_{23} compositions, there is a eutectic between RFe_3 and R_6Fe_{23}. For a peritectic reaction between RFe_3 and R_6Fe_{23}, the trough must lie at a composition with less iron than the RFe_3 phase.

The phase diagram in Figure 16 has come from the 0.7 Dy/0.3 Tb line (which represents that the rare earth component, R, consists of 70 at% Dy and 30 at% Tb). It can be seen from Figures 16 and 17 that for Terf 22.5 the R_2Fe_{17} phase is not expected under equilibrium conditions. Since the R_2Fe_{17} phase was observed in our samples, it seems that

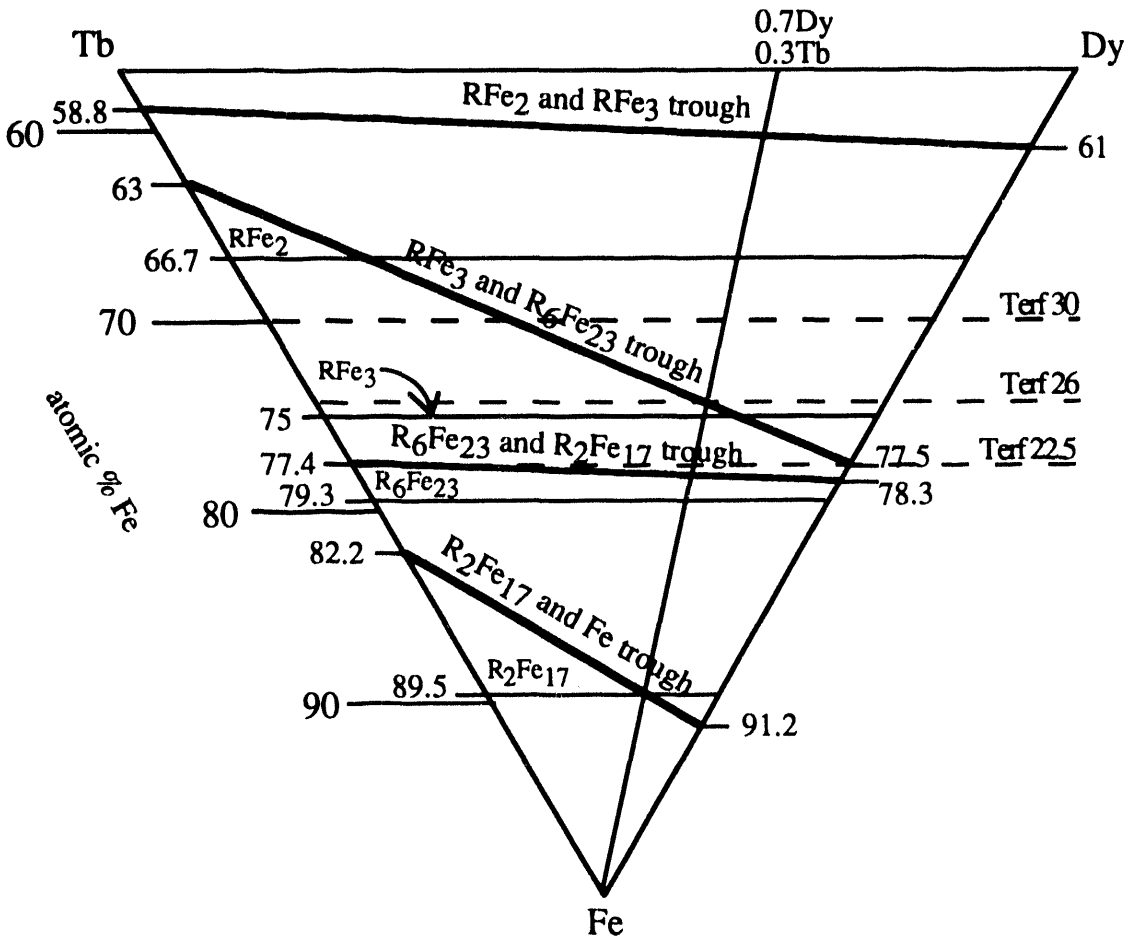

Figure 17 Fe-Dy-Tb ternary phase diagram viewed from above

either the trough line should be curved in Figure 17 (not a linear relationship) or that our samples did not solidify under equilibrium conditions. If the latter is so, then non-equilibrium precipitates form quite easily for these Terfenol alloys.

Also, from the calculation in Table 13, it is shown that an alloy of composition of 26.9 at % R (Dy:Tb = 7:3) will have equilibrium between RFe_3, R_6Fe_{23}, and liquid metal at a given temperature. Thus, an alloy of composition 26 at % R (Dy:Tb = 7:3) should form very little R_6Fe_{23} before the RFe_3 phase forms. However, our Terf 26 alloys showed considerable amounts of R_6Fe_{23}. This also implies that either the trough line should be curved in Figure 17 or that our Terf 26 samples did not solidify under equilibrium conditions.

CONCLUSION

Although the magnetostriction characteristics of Terfenol are outstanding, there is room for improvement. If we can control the dendritic growth of solidifying Terfenol, we may be able to grow a <111> oriented single crystal of Terfenol. Furthermore, the extensive research already conducted on Terfenol has not revealed its exact microstructure/stoichiometry relationship. With the research conducted, the ternary phase diagram of the Tb-Dy-Fe system in the Terfenol region has been outlined for a constant Dy:Tb ratio of 7:3. This information may be instrumental in defining the optimum stoichiometry and solidification conditions.

REFERENCES

1 Goodfriend, Mel, "High Magnetostrictive Alloy for Transducers and Actuators," *JOM*, p 1448-55, July, 1990.

2 Jiles, D. C., Introduction to Magnetism and Magnetic Materials, Chapman and Hall, London, 1991.

3 Clark, A. E. , Ferromagnetic Materials, "Magnetostrictive Rare Earth-Fe_2 Compounds," CH. 7, North-Holland Publishing Co., Amsterdam, 1980.

4 Verhoeven, J. D., E. D. Gibson, O. D. McMasters, and H. H. Baker, "The Growth of Single Crystal Terfenol-D Crystals," *Met. Trans A*, vol. 18A, Feb. 1987, pp. 223-231.

5 Verhoeven, J. D., E. D. Gibson, O. D. McMasters, and J. E. Ostenson, "Directional Solidification and Heat Treatment of Terfenol-D Magnetostrictive Materials," *Met. Trans. A*, vol. 21A, Aug. 1990, pp. 2249-2255.

6 Verhoeven, J. D. Fundamentals of Physical Metallurgy, John Wiley and Sons, New York, 1975, pp. 233-317.

7 McMasters, O. D., J. D. Verhoeven, and E. D. Gibson, "Preparation of Terfenol-D by Float-Zone Solidification," *Jour. Mag. and Mag. Mat.*, 54-57, 1986, pp. 849-850.

8 Massalski, Binary Alloy Phase Diagrams, ASM International, Materials Park, Ohio, Dec. 1990.

9 Bi, Y. J., J. S. Abell, and A. M. H. Hwang, "Defects in Terfenol-D Crystals," *Jour. Mag. and Mag. Mat.*, 99, 1991, pp. 159-166.

10 Porter, D. A., and K. E. Easterling, Phase Transformations in Metals and Alloys, V.N.R. International, London, 1981.

ACKNOWLEDGMENTS

I would like to acknowledge the guidance and assistance provided to me throughout my research endeavors. Foremost, I would like to thank Dr. J.D. Verhoeven as my major professor for all of his insight and for inspiring my research. I also extend many thanks to Mr. E.D. Gibson, who helped me a great deal with my experiments. I thank Mr. Paul M. Berge as a constant source of information. I would like to thank my husband, Alan, for his encouragement and support. I am also grateful to Mr. Hal Sailsbury for all of his time and patience. Mr. Seong Tcho Kim and Mrs. Patti Boone have always been so kind and helpful. And I would like to thank Dr. D.C. Jiles and Dr. D.K. Finnemore for taking the time to serve as committee members. To all of you, I offer my sincere appreciation for helping me achieve my goals.

This work was performed at Ames Laboratory under Contract No. W-7405-eng-82 with the U.S. Department of Energy. The United States government has assigned the DOE Report number IS-T 1688 to this thesis.

APPENDIX A. EQUIPMENT SETUP

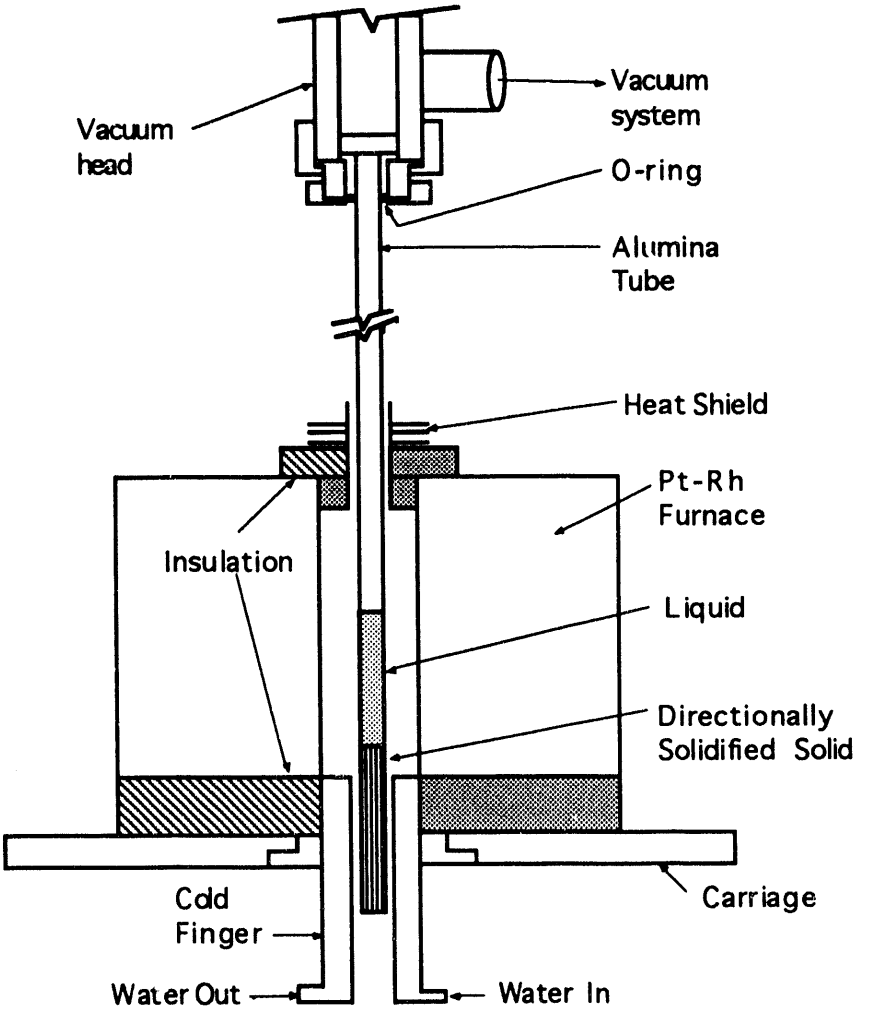

Figure 18 Schematic of the directional solidification furnace (courtesy of J. H. Lee)

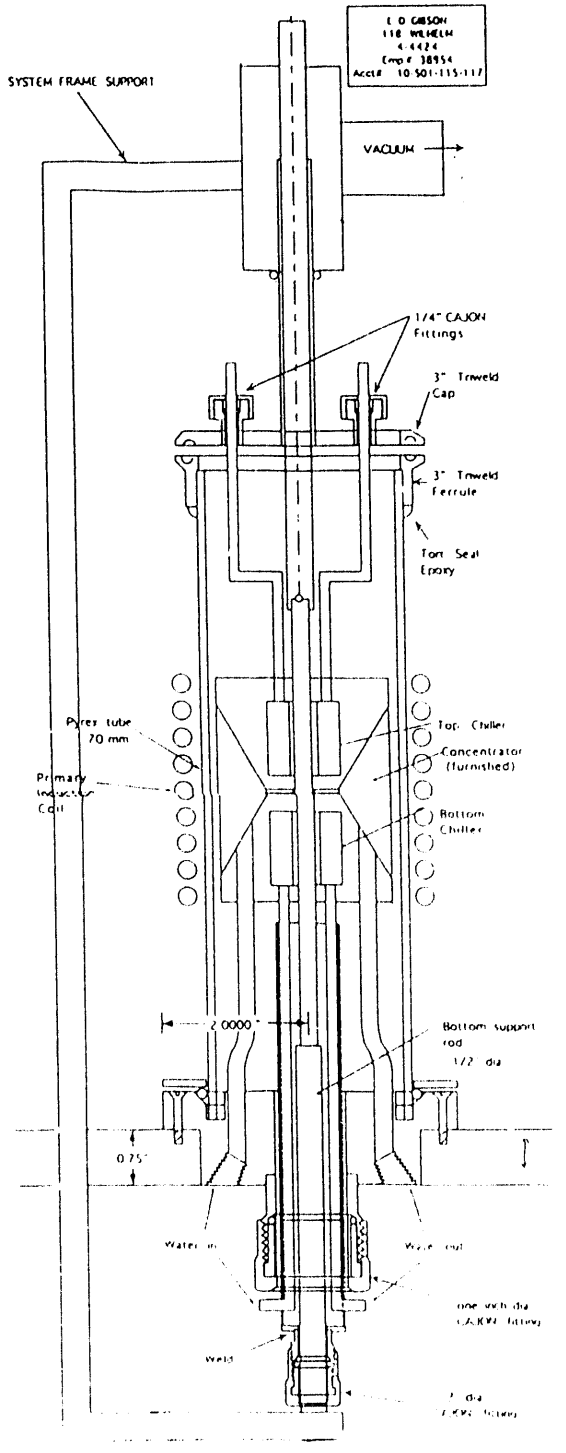

Figure 19 Schematic of the float zone solidification furnace (courtesy of E. D. Gibson)

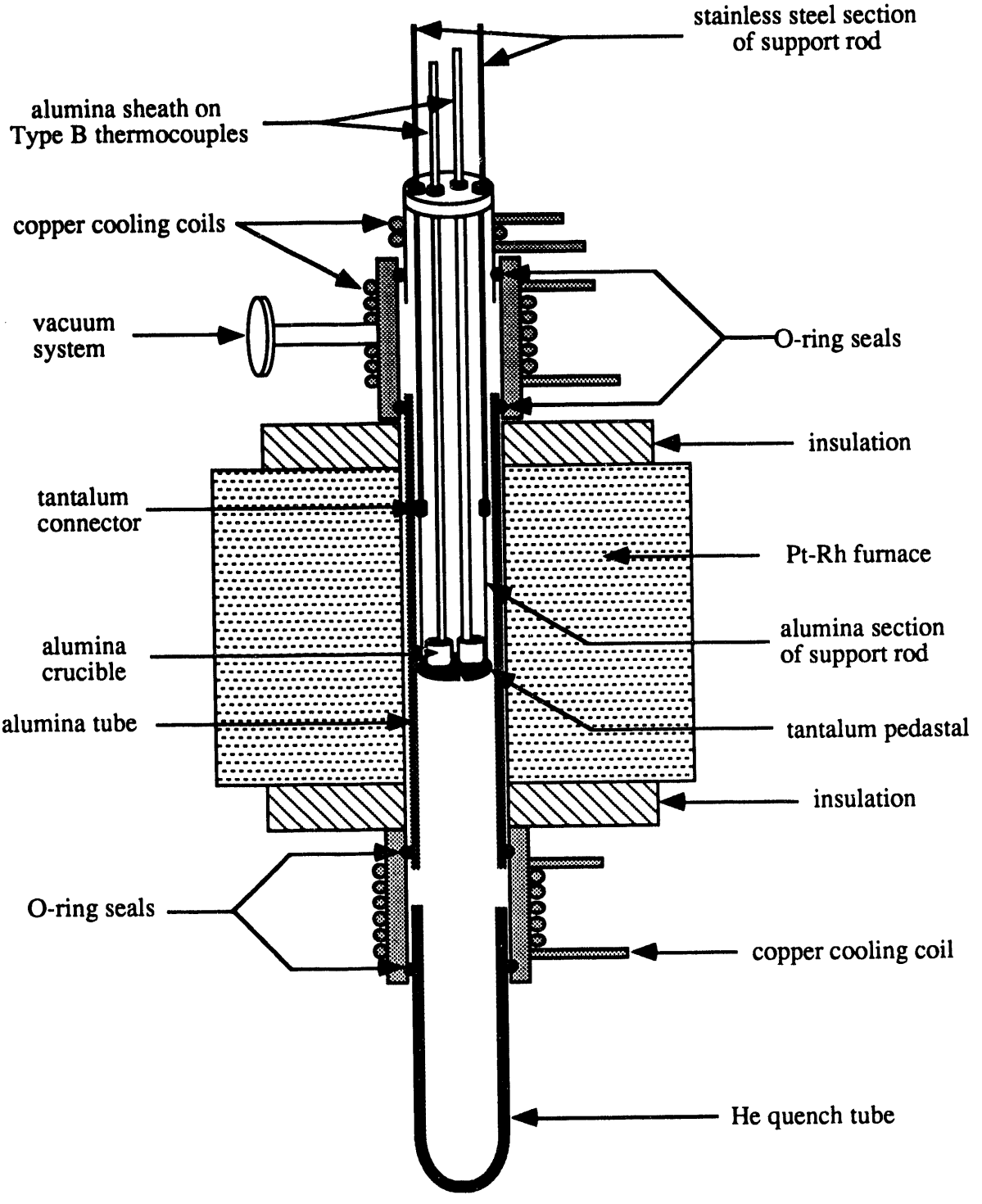

Figure 20 Schematic of the DTA furnace

APPENDIX B. TEMPERATURE GRADIENT INFORMATION

Assuming a unidirectional heat flow during solidification, the heat flow balance can be written as follows:

$K_S G_S = K_l G_l + LV$ (1)

at V = 0: $K_S G^\circ_S = K_l G^\circ_l$

and $K_S/K_l = G^\circ_l/G^\circ_S$

K_S = solid thermal conductivity
K_l = liquid thermal conductivity
G_S = solid thermal gradient
G_l = liquid thermal gradient
L = latent heat
V = velocity (velocity of furnace = solidification velocity)

and (1) can be arranged as:

$$K_l = \frac{LV}{\{(G^\circ_l/G^\circ_S)G_S - G_l\}} \quad ; \text{ forms: } G_l = \frac{K_S G_S - LV}{K_l} \qquad (2)$$

$$K_S = K_l(G^\circ_l/G^\circ_S) \qquad (3)$$

also, since Gs and Gl have a linear relationship with V,

$G_l = G^\circ_l + m_l V$ m_l = slope of G_l versus V

$G_S = G^\circ_S + m_S V$ m_S = slope of G_S versus V

By plotting the temperature gradient versus the solidification rate, G°l and G°s can be calculated for each furnace temperature and the average of these is used as G°s and G°l. Thus, the thermal conductivities can be calculated. For use in the Terfenol experiments, this technique was useful in determining the solidification velocity necessary to achieve large temperature gradients.

In order to determine the solidification rate required to grow part of a Terfenol rod with a planar growth front using directional solidification, it is necessary to use a mass balance of the rod as it is solidifying, as in Figure 20. From the mass balance:

$$[C_o - C_{cmpd}]\, Z = \{C_l - C_o\}\, (L - Z)$$

$$C_l - C_o = \frac{Z}{L - Z}\, [C_o - C_{cmpd}]$$

fraction solid = $f_S = Z/L$ fraction liquid = $f_l = (L - Z)/L$

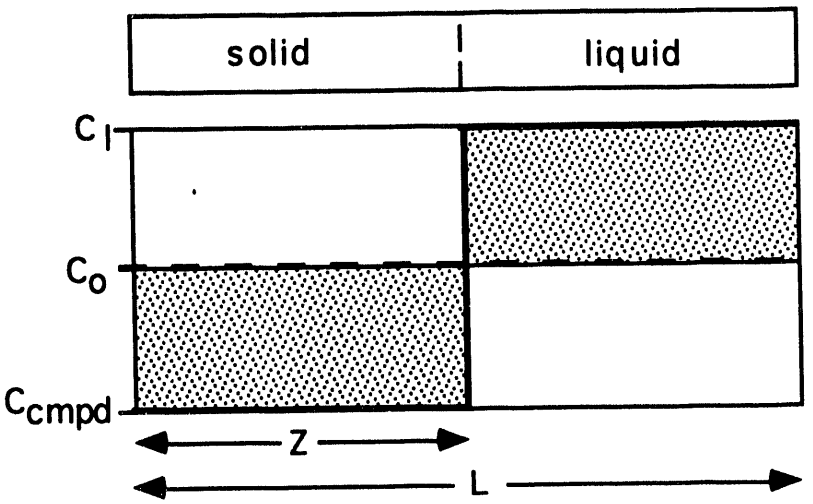

L = length of the melted rod (fixed)
Z = length of rod solidified (variable)
C_l = rare earth composition of the liquid (variable)
C_o = rare earth composition originally (fixed)
C_{cmpd} = rare earth composition of RFe_2 (fixed)

Figure 21 Schematic of the directional solidification of a Terfenol rod

$$C_l = C_o + \frac{f_s}{f_l} [C_o - C_{cmpd}]$$

$$C_l - C_{cmpd} = [C_o - C_{cmpd}] + \frac{f_s}{f_l} [C_o - C_{cmpd}]$$

$$C_l - C_{cmpd} = [C_o - C_{cmpd}] [1 + (f_s / f_l)]$$

$$C_l - C_{cmpd} = [C_o - C_{cmpd}] [1/f_l]$$

Adding this to the equation for the critical temperature gradient (temperature gradient above which dendrites will not form) yields:

$$G_{cr} = \frac{mR}{D} [C_l - C_{cmpd}] = \frac{mR}{D f_l} [C_o - C_{cmpd}]$$

where: m = slope of the liquidus on the phase diagram ≈ 10 °C/atom %
R = solidification rate = 10 and 2 μm/sec

D = diffusion rate = 2×10^{-5} cm^2/sec
C_o = original composition = 33.56 atom % rare earths
C_{cmpd} = compound composition = 33.33 atom % rare earths

Solving for both rates:

at R = 2 μm/sec, $G_{cr} = \frac{23}{f_l}$ °C/cm

at R = 10 μm/sec, $G_{cr} = \frac{115}{f_l}$ °C/cm

For a six inch rod (≈ 15 cm), the rate required to get 1/4 of the rod dendrite-free is:

at R = 2 μm/sec, G_{cr} = 13 °C/cm

at R = 10 μm/sec, G_{cr} = 153 °C/cm

Some of the temperature gradients from direction freezing experiments using Terfenol are given in Table 14. From preliminary calculations of the minimum temperature gradient required to suppress dendritic growth, it was determined that at a solidification rate of 10 microns/sec the critical temperature gradient, G_{cr}, would be 153°C/cm, and G_{cr} for a 2 micron/sec rate would be 31 °C/cm. As can be seen in Table 14, the temperature gradient did not exceed 153°C/cm at a 10 micron/sec solidification rate.

Table 14 Liquid and solid temperature gradients of Terfenol ($Tb_{.31}Dy_{.69}Fe_{1.98}$) from a furnace temperature of 1350 °C

Rate:	Exp. liq gradient	MBH-1-51 sol gradient	T melt
(um/sec)	(°C/cm)	(°C/cm)	(°C)
5	36.2	63.3	1234
10	34.9	64.7	1235
25	32.4	65.1	1238
50	32.8	69.2	1235

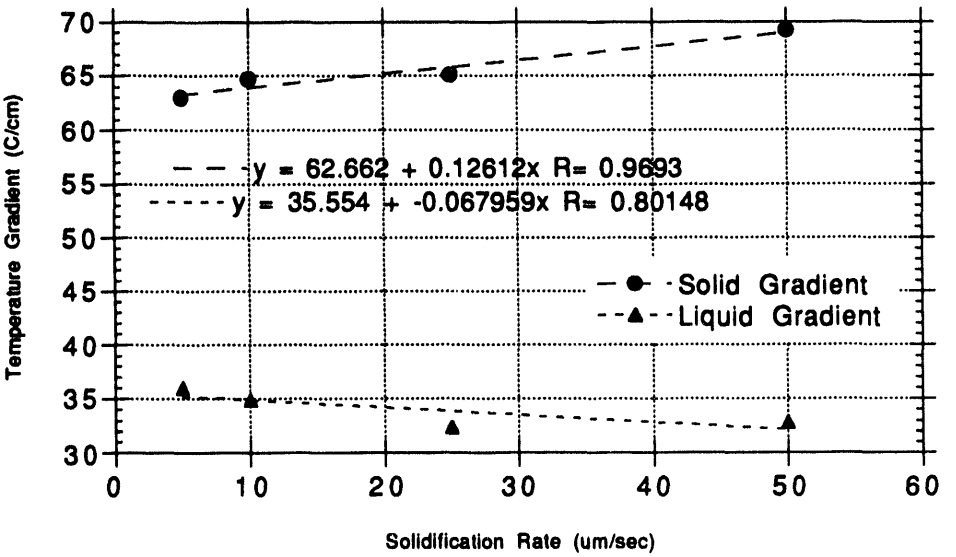

Figure 22 Temperature gradient versus solidification rate for Terfenol directionally solidified from a furnace temperature of 1350°C at rates of 5, 10, 25, and 50um/sec

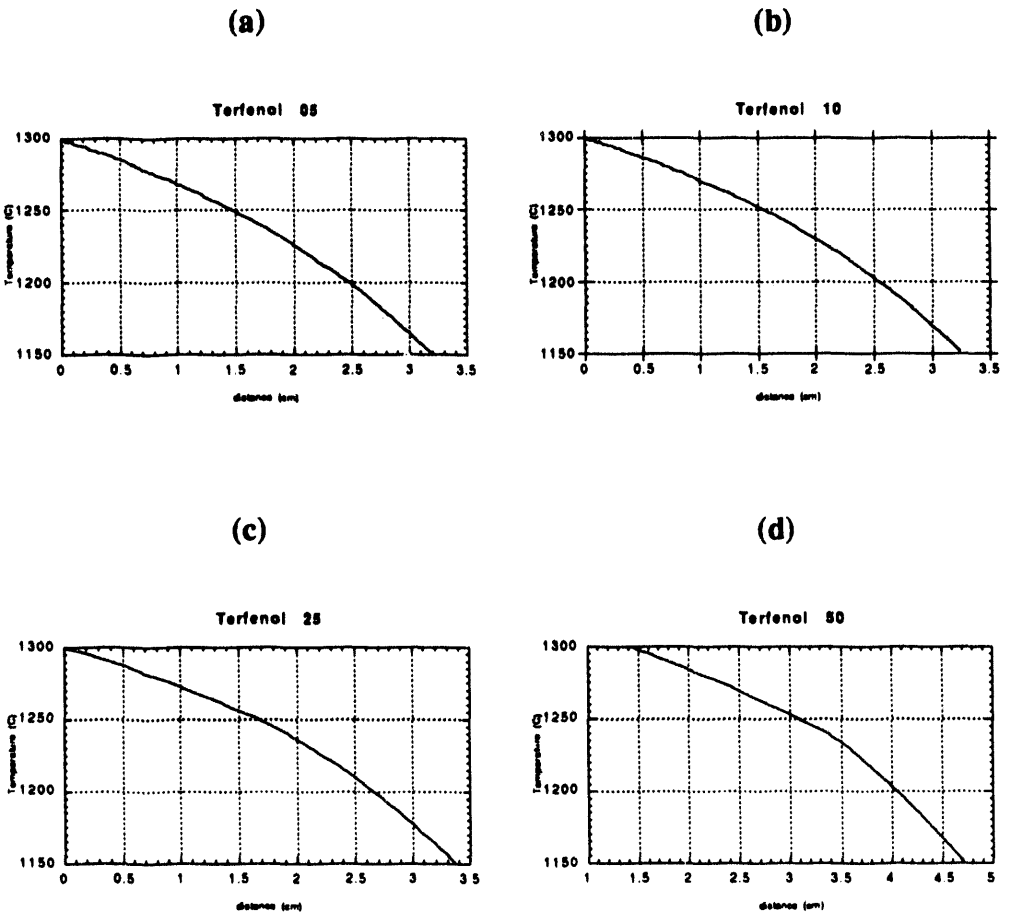

Figure 23 Temperature vs. distance plots directional solidification of Terfenol (1350°C furnace at solidification rates of **(a)** 5, **(b)** 10, (c) 25, and **(d)** 50 um/sec)

APPENDIX C. DTA PLOTS

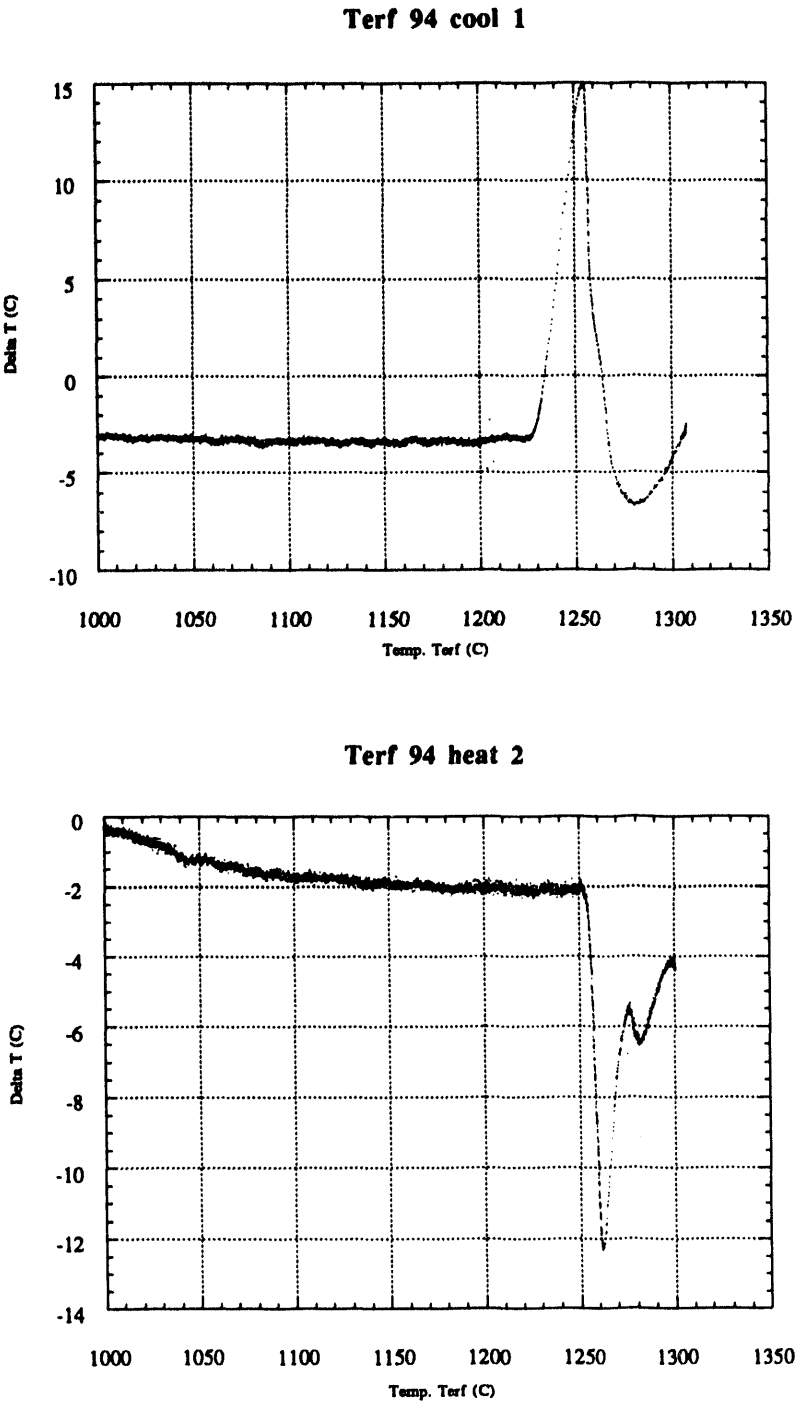

Figure 24 Cool and reheat at 5°C/min from differential thermal analysis performed on Terf 22.5 in experiment set 1 (experiment 1-79)

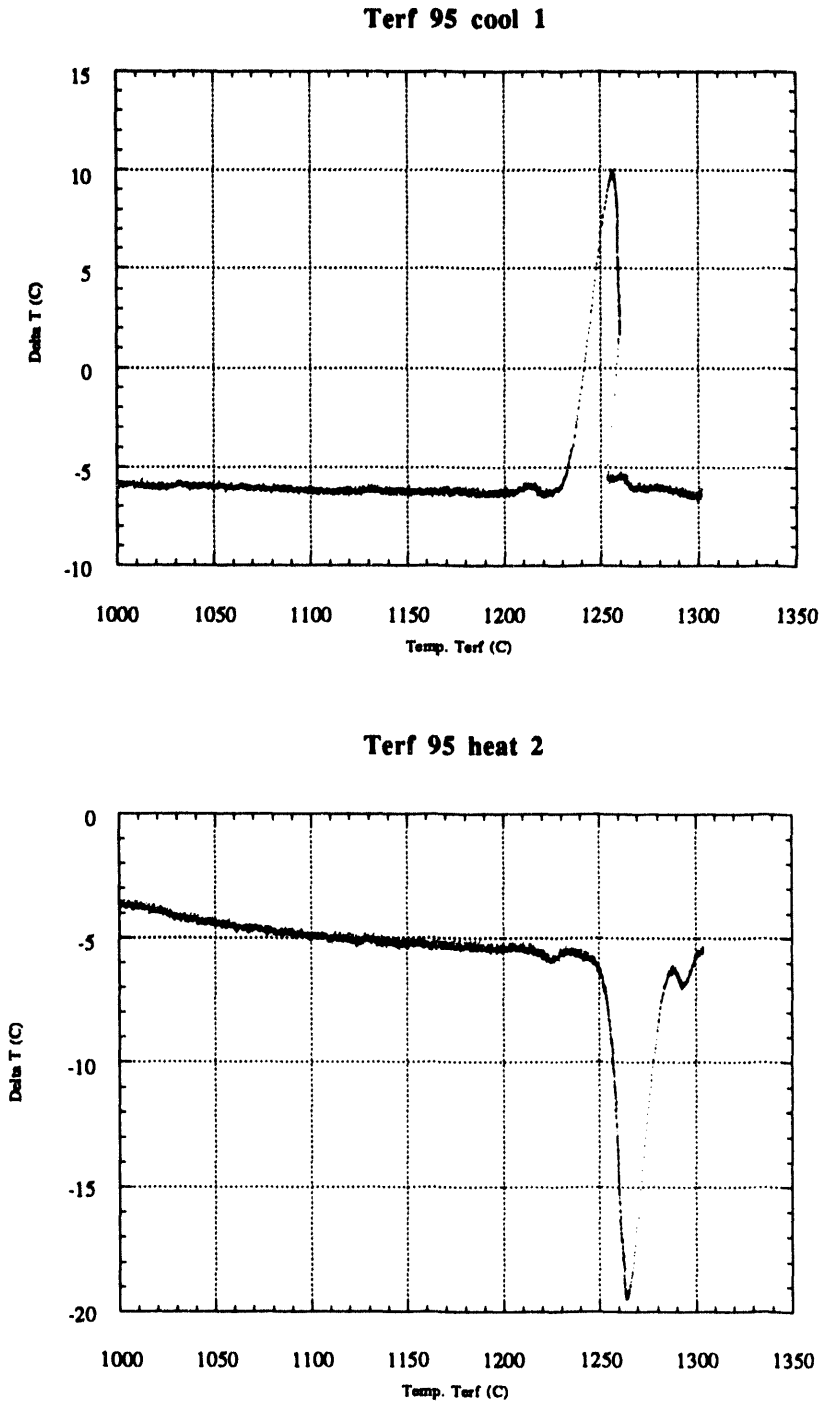

Figure 25 Cool and reheat at 5°C/min from differential thermal analysis performed on Terf 26 in experiment set 1 (experiment 1-81)

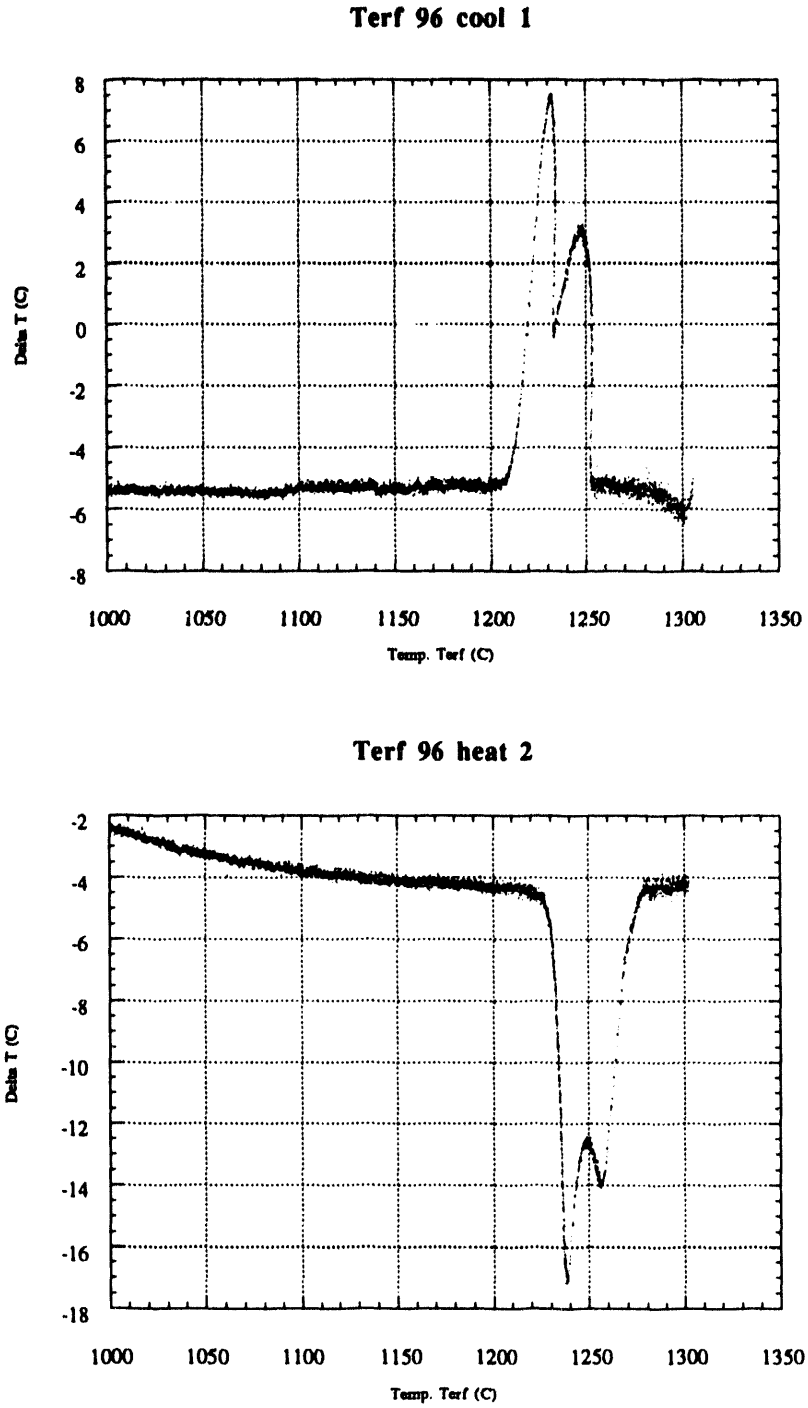

Figure 26 Cool and reheat at 5°C/min from differential thermal analysis performed on Terf 30 in experiment set 1 (experiment 1-83)

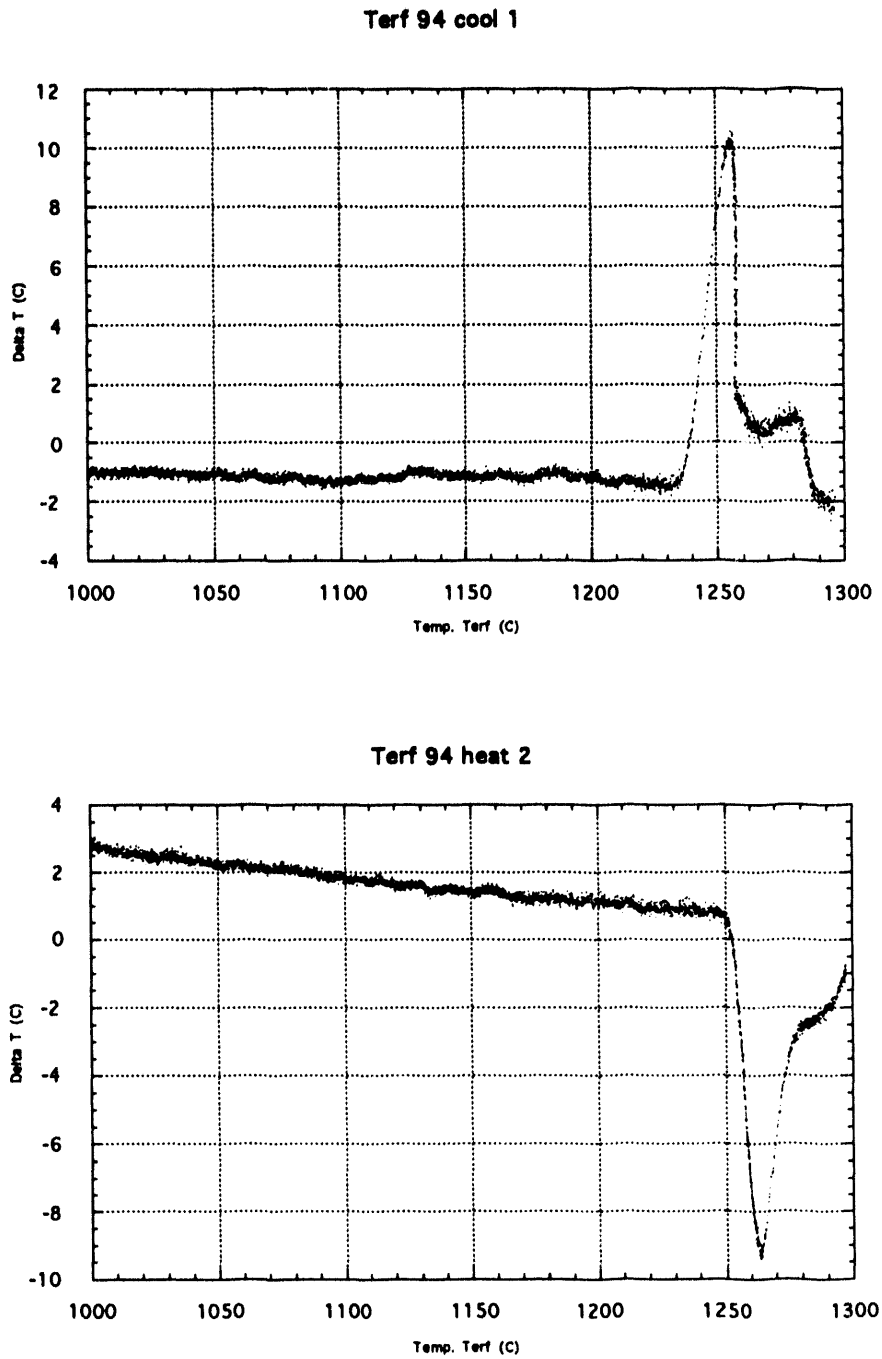

Figure 27 Cool and reheat at 5°C/min from differential thermal analysis performed on Terf 22.5 in experiment set 2 (experiment 1-85)

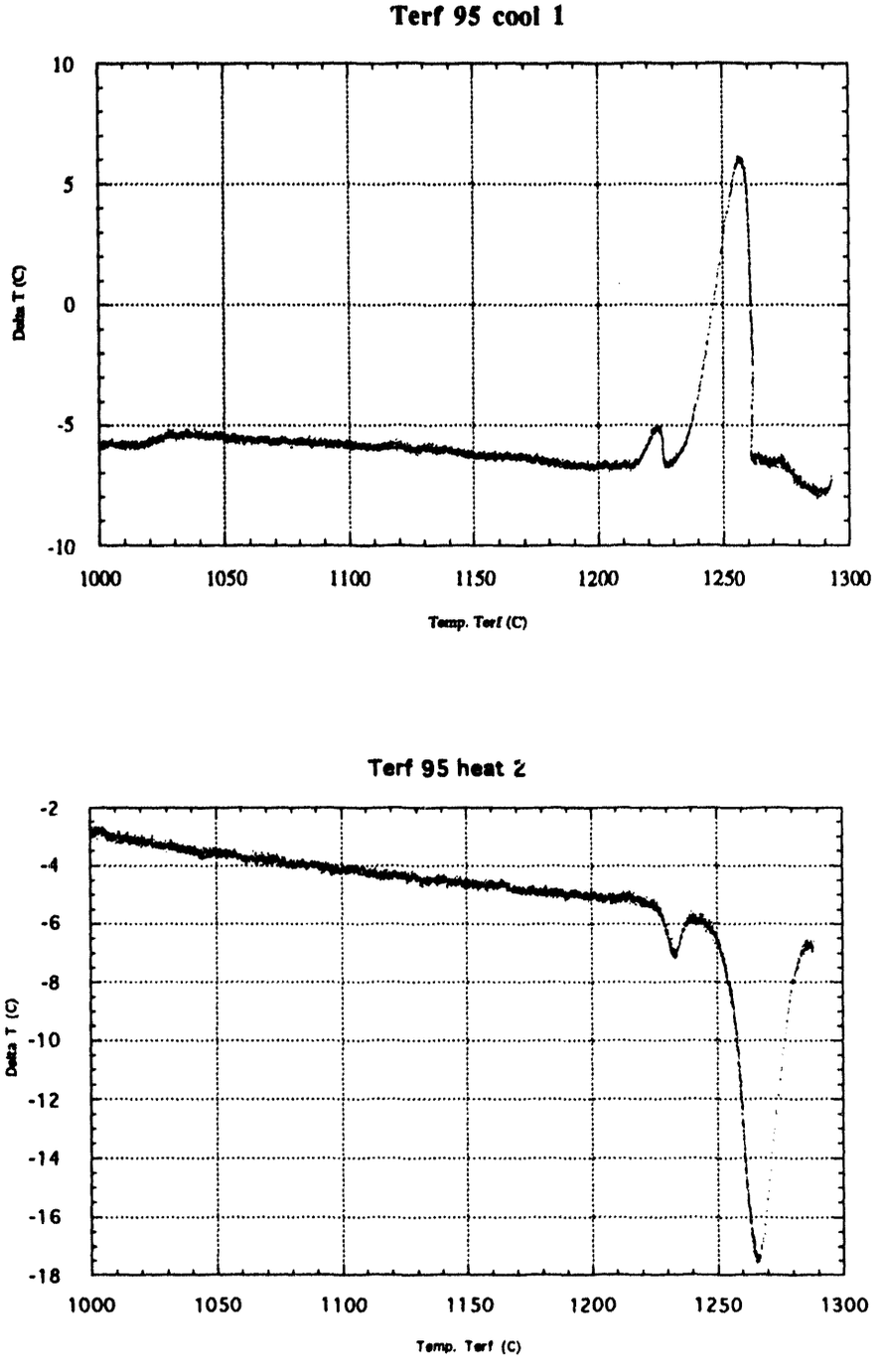

8Figure 26 Cool and reheat at 5°C/min from differential thermal analysis performed on Terf 26 in experiment set 2 (experiment 1-87)

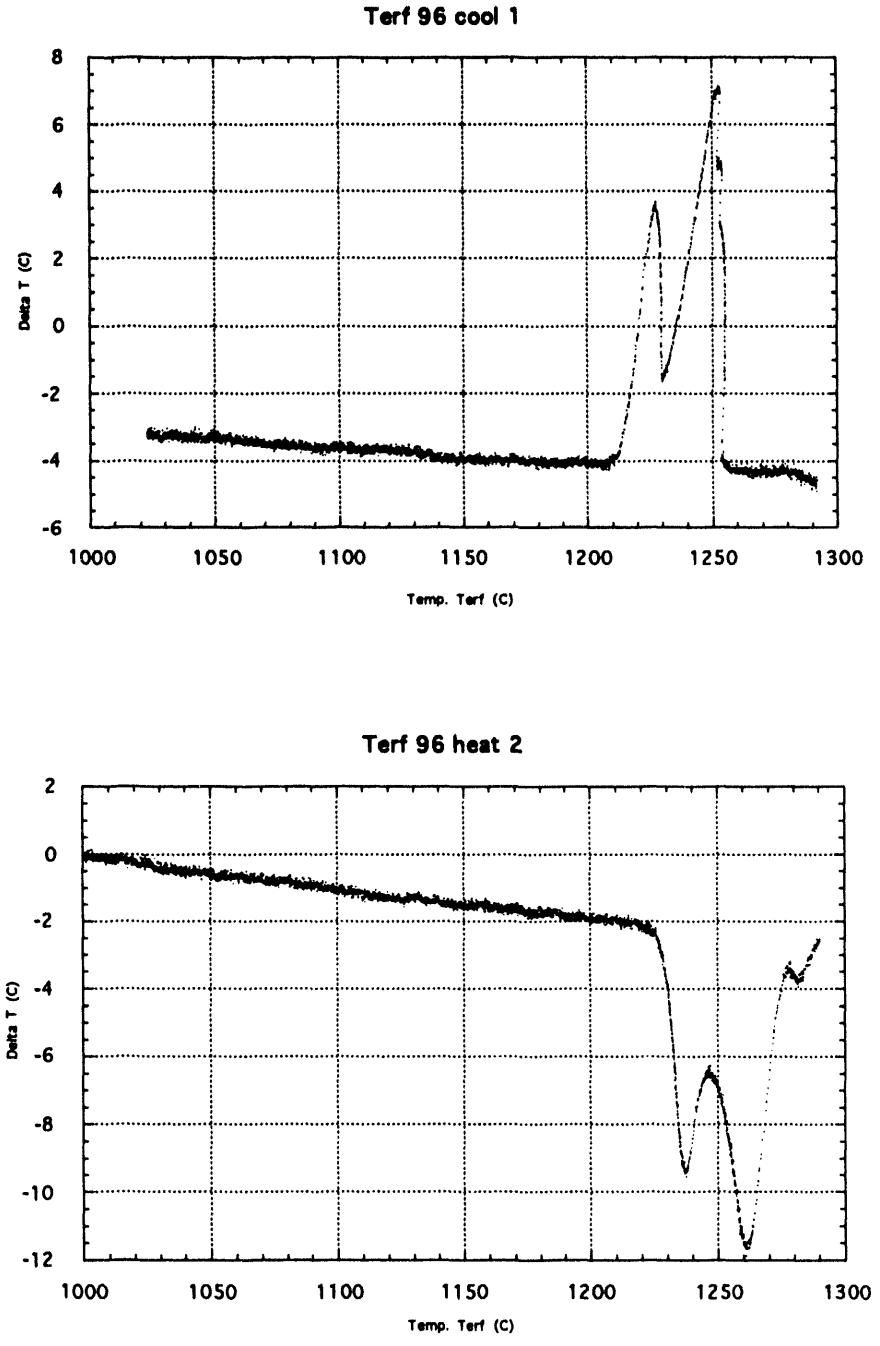

Figure 29 Cool and reheat at 5°C/min from differential thermal analysis performed on Terf 30 in experiment set 2 (experiment 1-89)

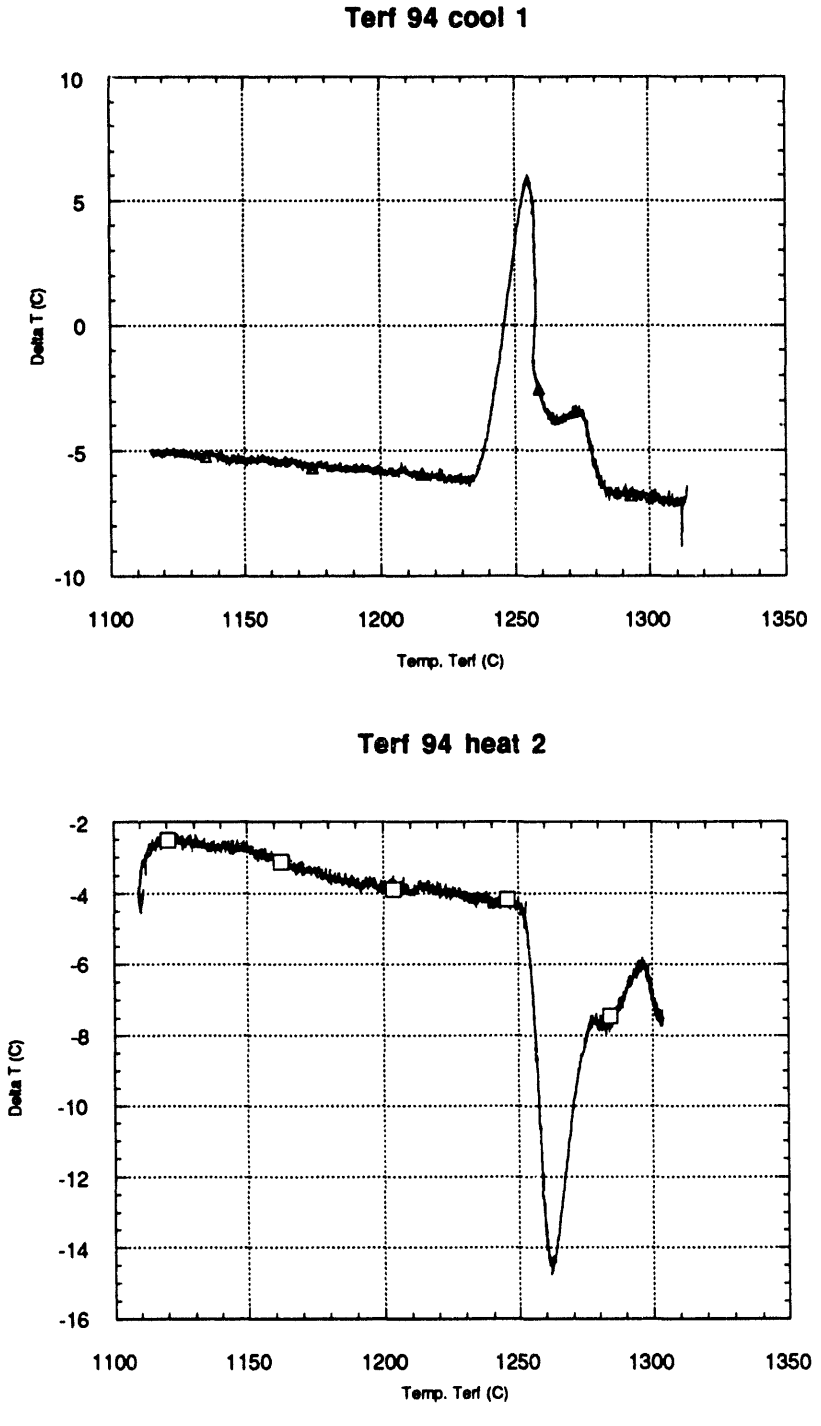

Figure 30 Cool and reheat at 5°C/min from differential thermal analysis performed on Terf 22.5 in experiment set 3 (experiment 1-91)

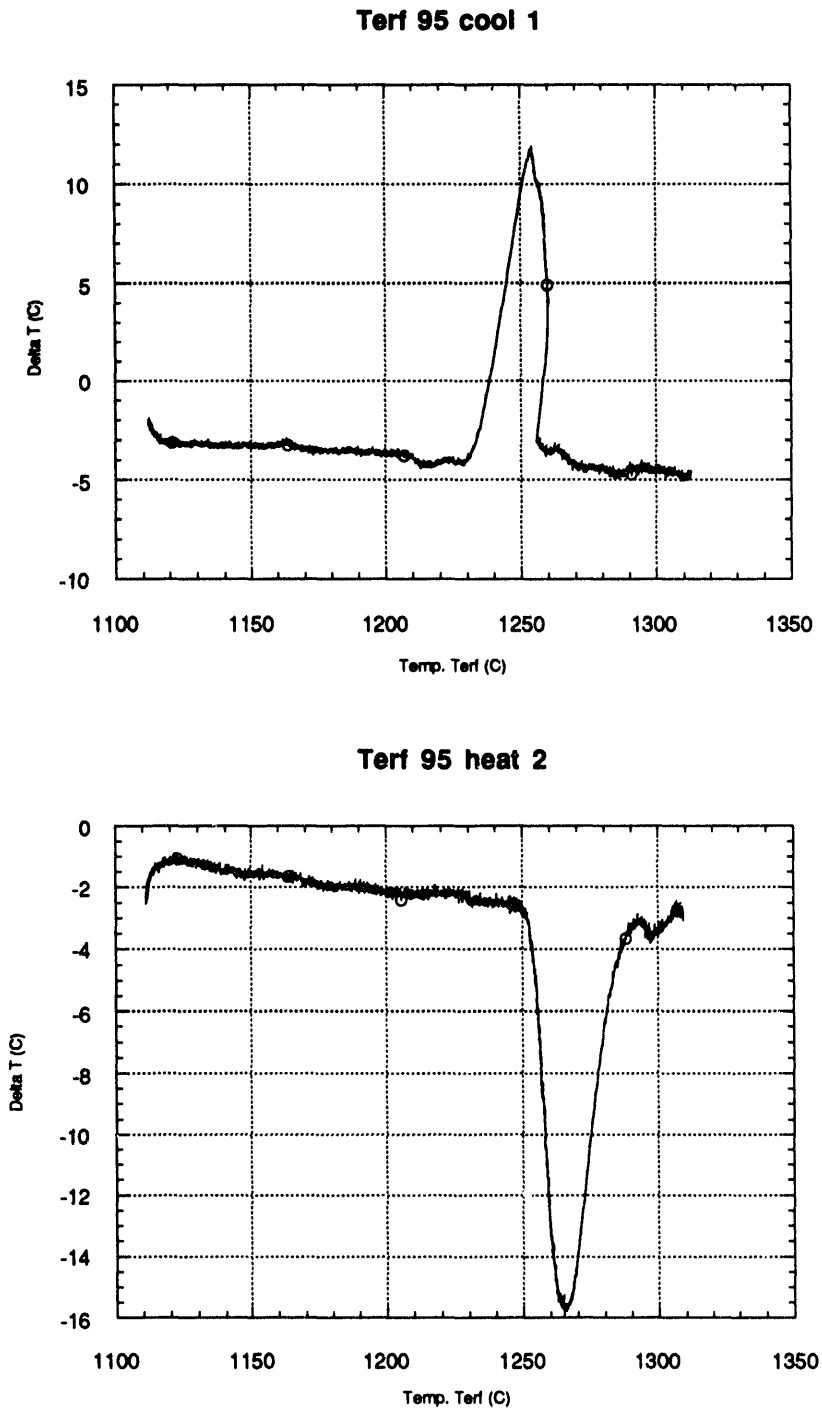

Figure 31 Cool and reheat at 5°C/min from differential thermal analysis performed on Terf 26 in experiment set 3 (experiment 1-93)

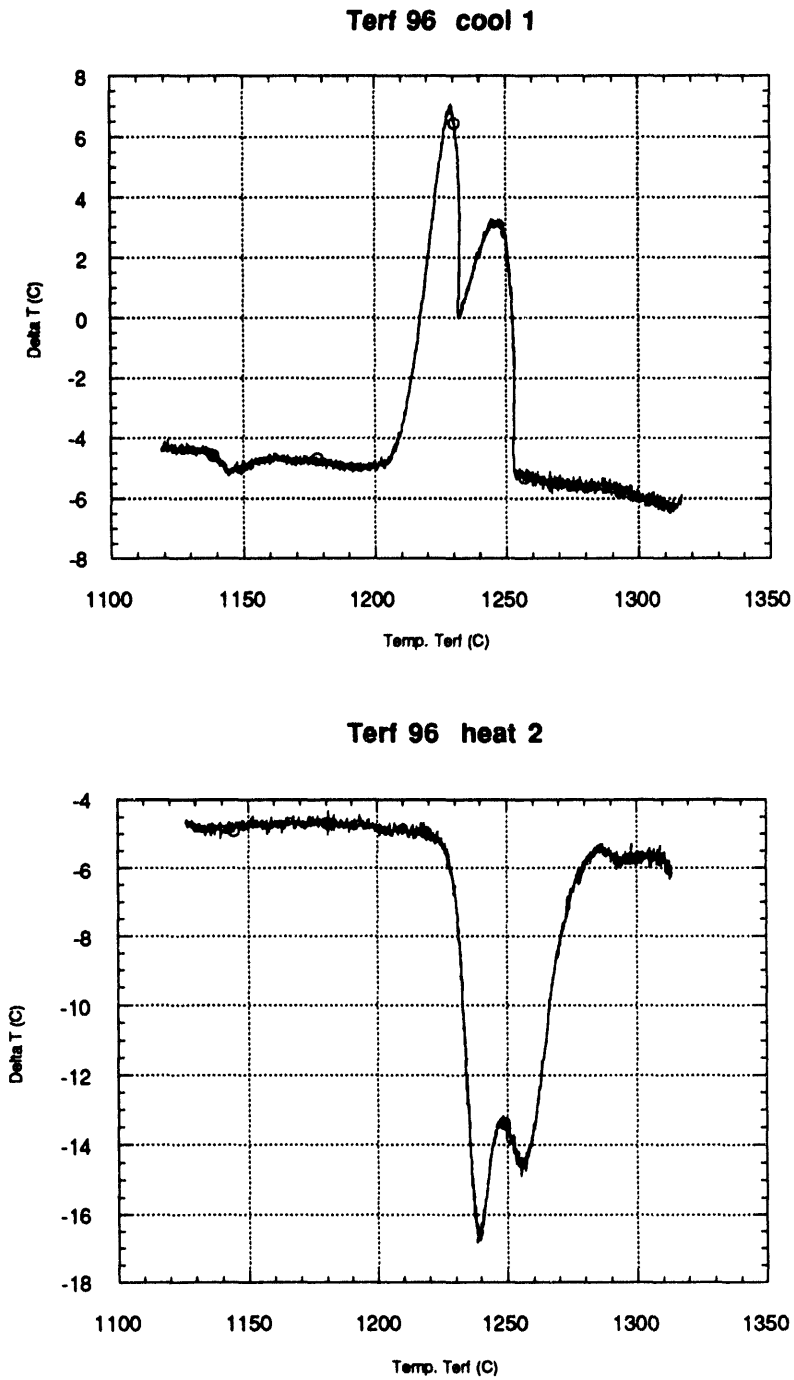

Figure 32 Cool and reheat at 5°C/min from differential thermal analysis performed on Terf 30 in experiment set 3 (experiment 1-95)

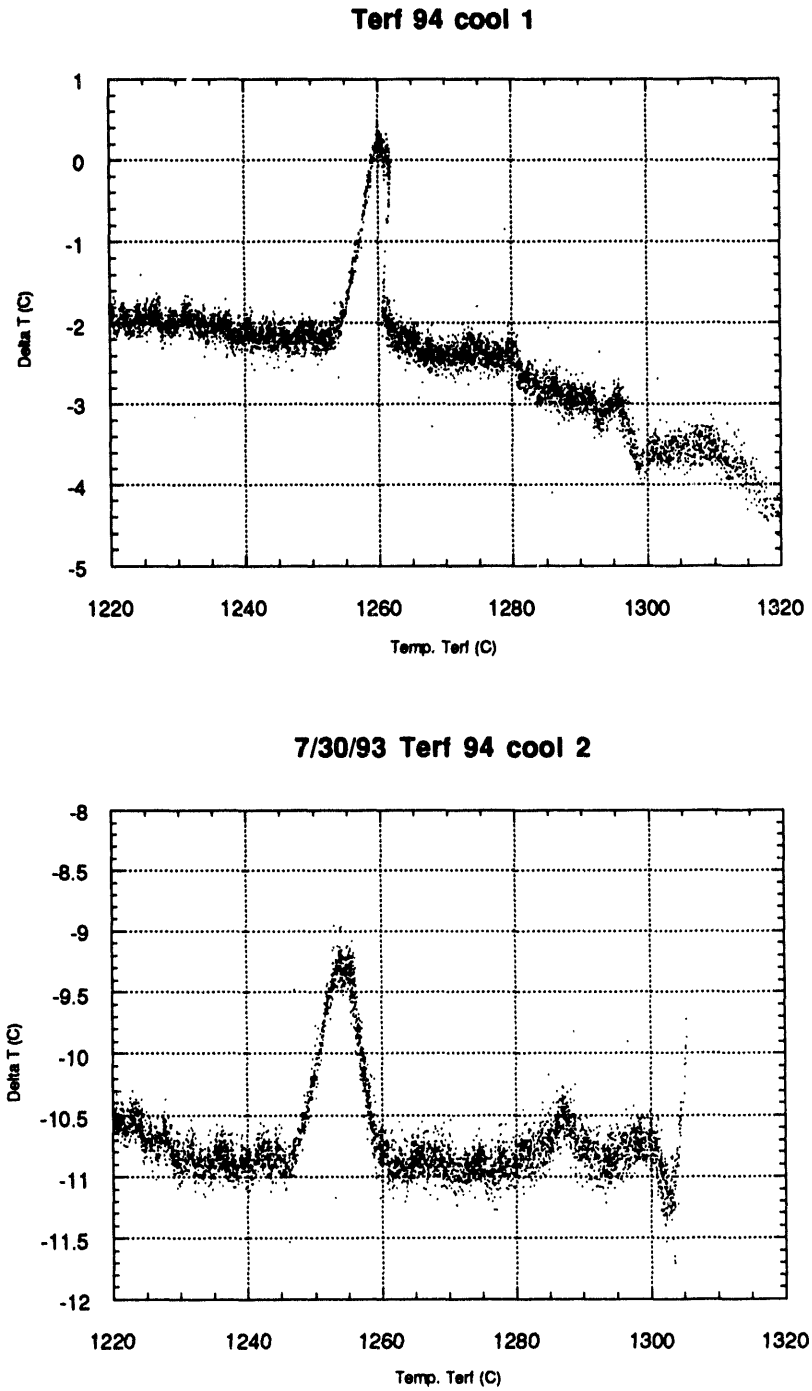

Figure 33 Two cools at 1°C/min from differential thermal analysis performed on Terf 22.5 in experiment set 4 (experiment 1-99)

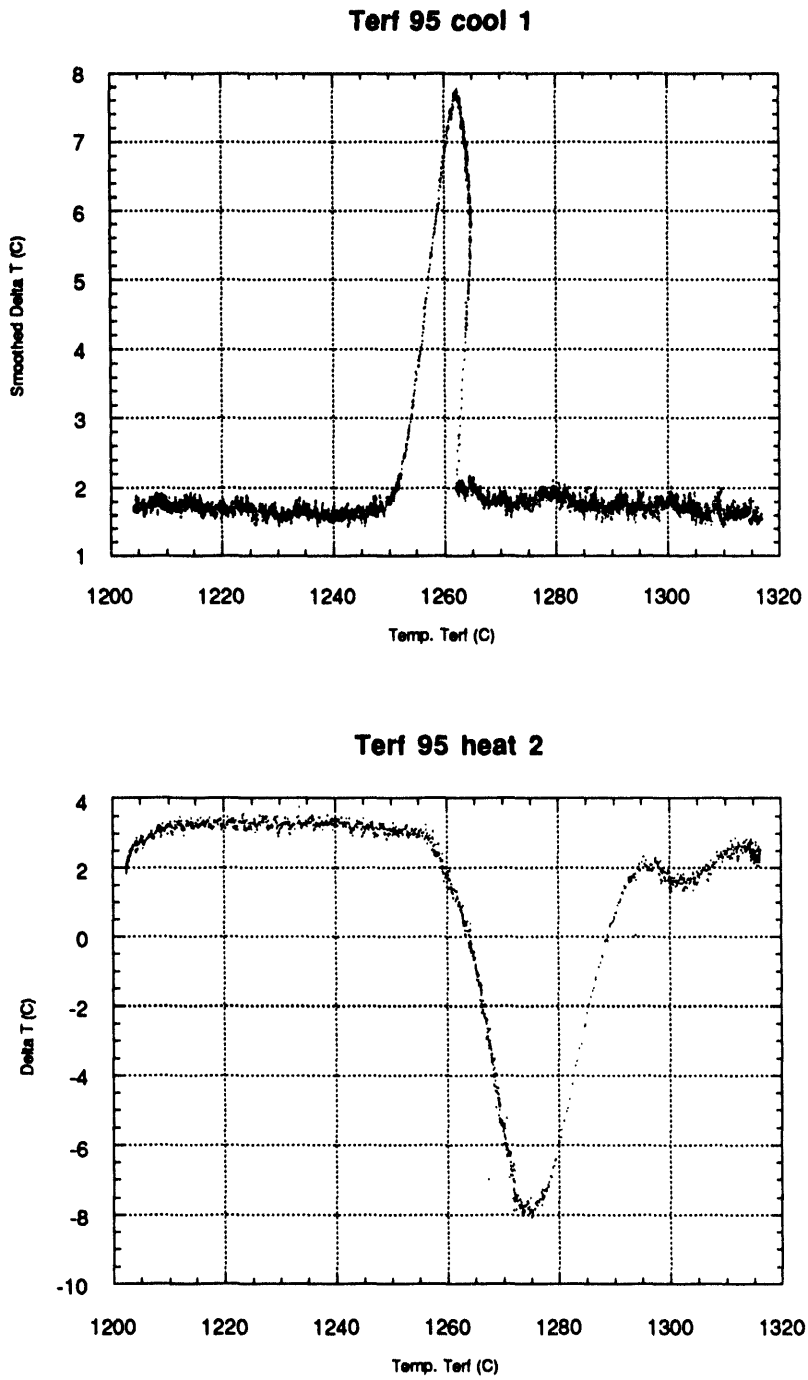

Figure 34 Cool at 1°C/min and reheat at 5°C/min from differential thermal analysis performed on Terf 26 in experiment set 4 (experiment 1-101)

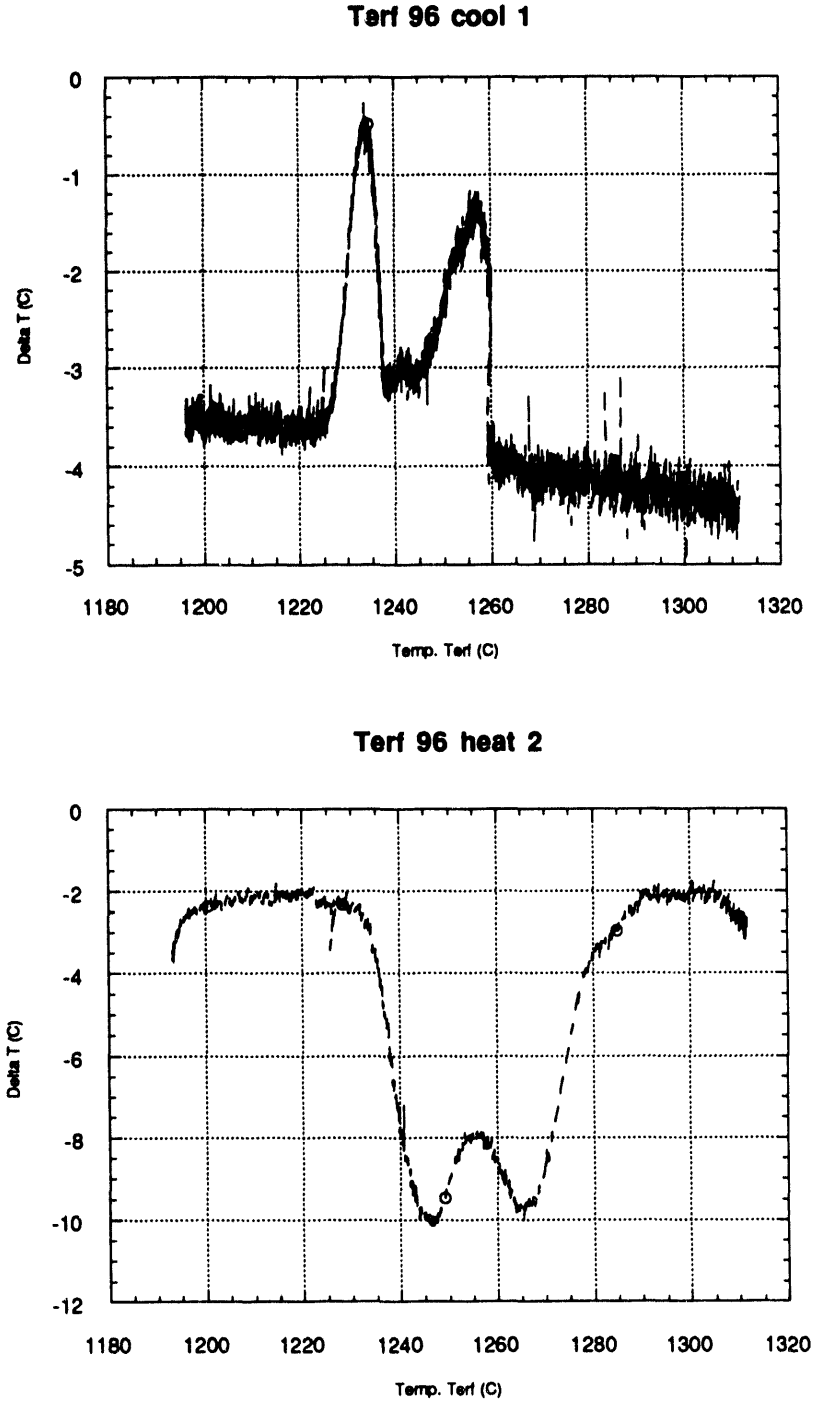

Figure 35 Cool at 1°C/min and reheat at 5°C/min from differential thermal analysis performed on Terf 30 in experiment set 4 (experiment 1-103)

APPENDIX D. PHOTOMICROGRAPHS

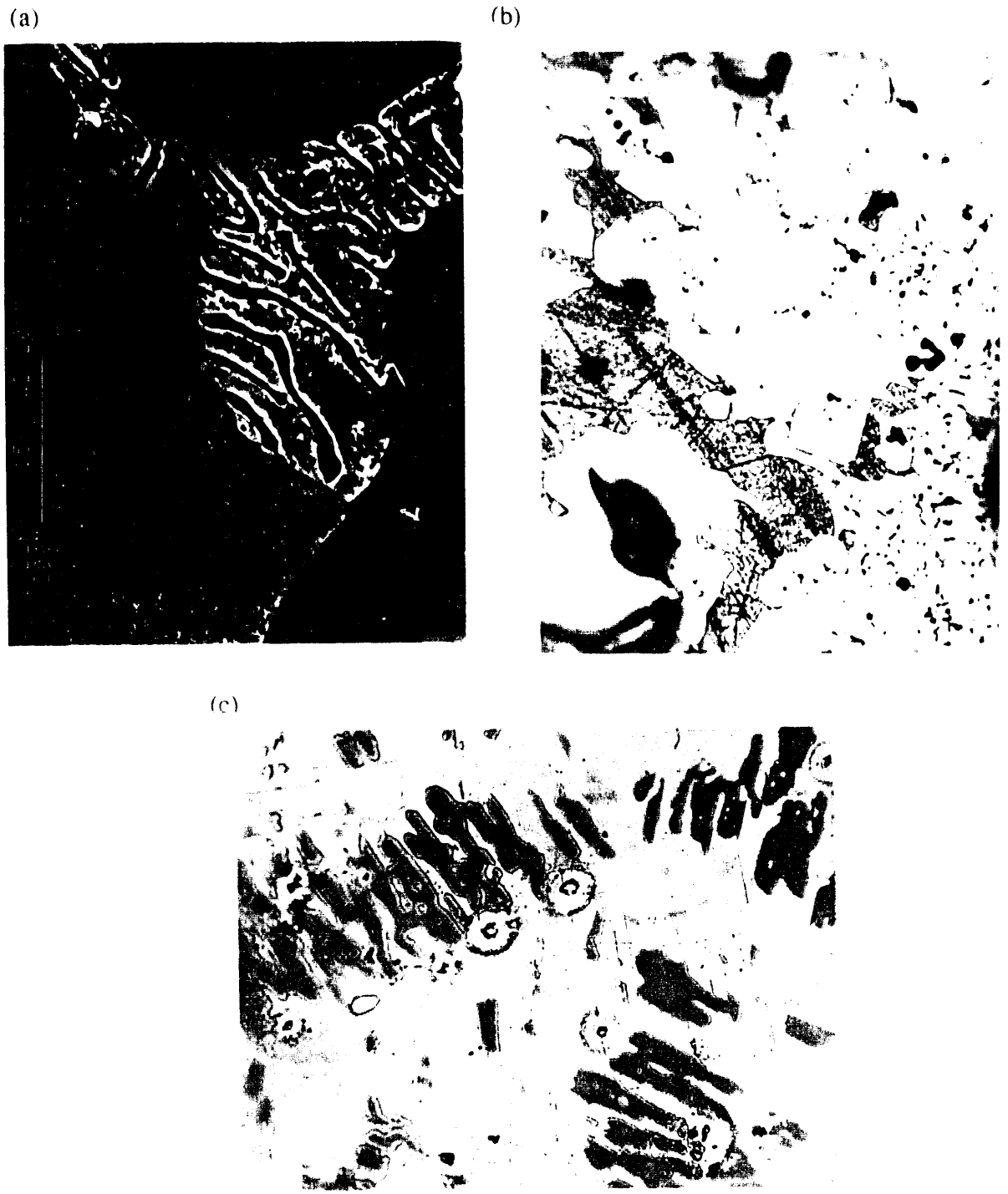

Figure 36 Photomicrographs of Terf 2.5 solidified at (a) 1 °C/min, (b) 5 °C/min, and (c) furnace cooled (≈26 °C/min)

(a)

(b)

Figure 37 Photomicrographs of Terf 26 solidified at (a) 1 °C/min and (b) 5 °C/min

(a)

(b)

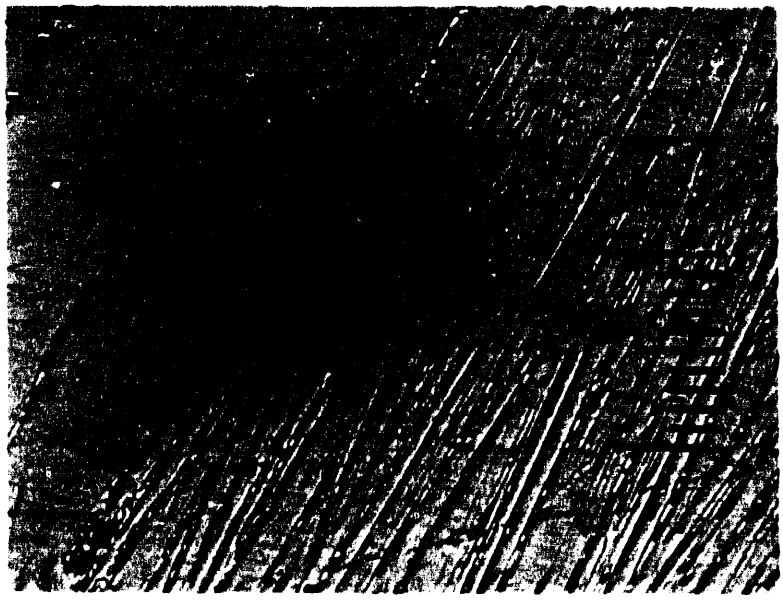

Figure 38 Photomicrographs of Terf 26 solidified by (a) furnace cooling (≈26 °C/min) and (b) quenching in a helium atmosphere

(a)

(b)

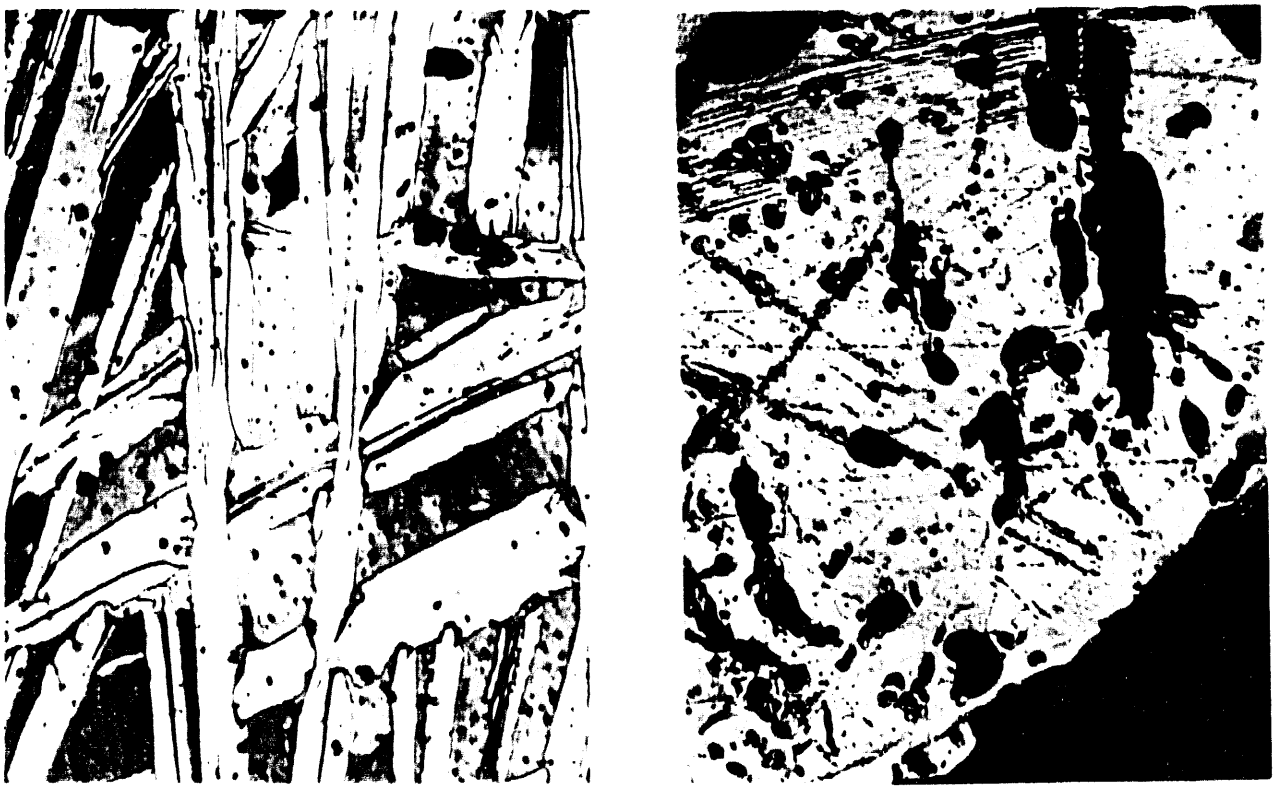

(c)

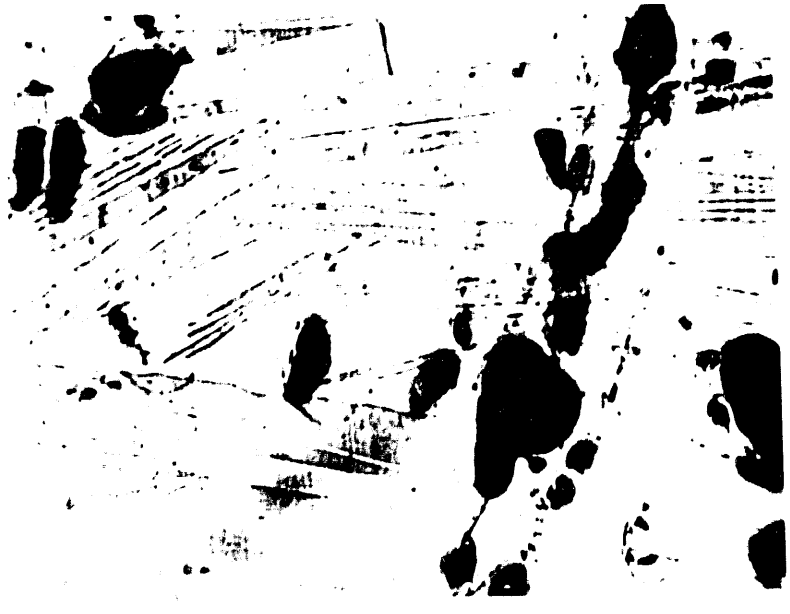

Figure 39 Photomicrographs of Terf 30 solidified at (a) 1 °C/min, (b) 5 °C/min, (c) furnace cooled (≈26 °C/min)

DATE
FILMED
2/23/94
END